International Journal of Heat and Mass Transfer 123 (2018) 297–319

Contents lists available at ScienceDirect

International Journal of Heat and Mass Transfer

journal homepage: www.elsevier.com/locate/ijhmt

Direct Numerical Simulation of an air-filled differentially heated square cavity with Rayleigh numbers up to 10^{11}

Frederic Sebilleau [a], Raad Issa [a,*], Sylvain Lardeau [b], Simon P. Walker [a]

[a] Imperial College London, Department of Mechanical Engineering, SW7 2AZ, UK
[b] CD-Adapco, 200 Shepherds Bush Road, London W6 7NL, UK

ARTICLE INFO

Article history:
Received 17 January 2018
Received in revised form 12 February 2018
Accepted 12 February 2018
Available online 20 March 2018

Keywords:
DNS
Buoyancy driven flows
Differentially heated cavity
Reynolds stress budgets

ABSTRACT

A set of Direct Numerical Simulations in a heated square cavity invoking the Boussinesq approximation was carried out at Rayleigh numbers ranging between 10^8 and 10^{11} and Prandtl number of 0.71. The three dimensional configurations studied represent an infinitely deep cavity, thus corresponding to a statistically two-dimensional flow with an imposed temperature varying linearly on the horizontal walls. In such configuration, the Rayleigh number, and therefore turbulence intensity, is the highest ever reached. The database presented herein includes first and second order statistical moments as well as full Reynolds stresses, turbulent heat fluxes and temperature variance budgets. The latter are extremely rare for buoyancy driven flow configurations and are therefore believed to be valuable to the turbulence modelling community. The analysis of the data collected thus focuses on aspects of relevance to the Reynolds averaged modelling of such flows. The effect of increasing the Rayleigh number on the flow statistics, Nusselt number predictions and thermal stratification is investigated. The most important aspect influencing the behaviour of the budgets was found to be the displacement of the position of the maximum of temperature variance towards the inner zone of the boundary layer. Such difference in behaviour between the thermal and velocity boundary layers introduces regions of negative production in the budgets that tend to increase with the Rayleigh number. The production of turbulence by buoyancy is also found to be of the same order of magnitude as other budget terms at all Rayleigh numbers.

1. Introduction

Buoyancy-driven flows are ubiquitous in the environment as well as in many industrial configurations. Common examples of such industrial applications include double-glazed windows, passive cooling systems for electronic components and possibly nuclear reactor emergency cooling systems. Rectangular differentially heated cavities have the advantage to be very simple from a geometrical point of view whilst embodying complex physics of interest: spatially developing buoyant boundary layers in the presence of thermal stratification. The present paper focuses on cavities where the main temperature difference is applied between the vertical walls, yielding a mean horizontal gradient of temperature between the walls. This case is different from the Rayleigh-Bénard type convection where the temperature gradient is aligned with the gravity vector in an unstable manner. The purpose of the present work is to provide an analysis of the physics of buoyancy driven flow in a differentially heated cavity with a Reynolds averaged modelling perspective. Rectangular vertical differentially heated cavities have been a topic of interest for decades now. The work of Batchelor [1], who studied analytically the limiting case of very tall cavities at low Rayleigh number, was the first on the topic. Other early studies such as the pioneering work by Elder [2,3] on high aspect ratio cavities were mainly experimental and focused on the identification of the different flow regimes obtained when varying the Rayleigh and Prandtl number. Three flow regimes were identified experimentally: steady laminar flow, unsteady laminar flow and fully turbulent flow. A large body of work has been focused on the characterisation of such flow regimes as a function of the dimensionless numbers governing the flow. When the fluid satisfies the Boussinesq approximation, a simple normalisation of each term of the Navier-Stokes equation shows that the flow is fully characterised by the Rayleigh number, the Prandtl number and the aspect ratio of the cavity. Due to the limited computational resources, numerical solutions of differentially heated cavity flows were originally limited to very low Rayleigh number well within the laminar regime. These early calculations were two-dimensional, usually based on the streamfunction-vorticity formulation of the Navier-Stokes

* Corresponding author.
E-mail address: r.issa@imperial.ac.uk (R. Issa).

https://doi.org/10.1016/j.ijheatmasstransfer.2018.02.042
0017-9310/

equations and relying on the Boussinesq approximation to account for buoyancy effects on the flow [4,5]. Most of the numerical results obtained in the laminar regime were consistent with each other. For instance, the results obtained by De Vahl Davis [6] using Richardson's extrapolation for a square cavity with Rayleigh number between 10^3 and 10^6 are still widely used for code validation purposes. Other studies such as the work of Chenoweth and Paolucci [7] studied the behaviour of the flow in cavities of various aspect ratio with variable fluid properties. They observed that the flow loses its centro-symmetry when departing from a Boussinesq-type fluid and proposed flow regime maps. Much attention in the literature has been paid to the identification of the mechanisms triggering the transition to unsteadiness and later to turbulence. This was initially done by studying the stability of two-dimensional solution of the Navier-Stokes equation [8,9] when introducing small perturbations. It was later shown by Henkes and Le Quéré [10] that the critical Rayleigh number was lower when considering a three-dimensional cavity with periodic boundary conditions in the third direction and applying a three-dimensional perturbation. The critical Rayleigh number was found to depend on the aspect ratio of the cavity [8] and also on the boundary conditions applied to the horizontal walls. Two classic extreme configurations can be found in the literature: adiabatic horizontal wall and perfectly conducting ones (linear variation of temperature between hot and cold side of the cavity), with the former representing the vast majority. Henkes and Le Quéré [10] showed that the critical Rayleigh number for the conducting square cavity is around 2×10^6 whereas the more recent study of Xin and Le Quéré [11] showed that the critical Rayleigh number in an adiabatic three-dimensional square cavity is around 1.55×10^7, which is more than one order of magnitude lower than the critical Rayleigh number observed by the same authors in the two-dimensional case. As regards the fully turbulent flow regime, numerical analysis by Direct Numerical Simulation (DNS) has been impossible for a very long time because of the limited computational resources available and the particular complexity of the problem. Indeed, differentially heated cavity flows often have, in their fully turbulent regime, a quiescent stratified core and very thin buoyant boundary layers along the walls, which demand large computational resources. A very large number of early studies considered the two-dimensional form of the Navier-Stokes equation in the fully turbulent regime [12,9]. It is only in the last decade that accurate solution of the three dimensional problem emerged, firstly with the publication of increasingly resolved large-eddy simulations (LES) [13,14], supported by the publication of experimental data [15–17] followed by direct numerical simulations. A large number of direct numerical simulations in tall differentially heated cavities (aspect ratios between 4 and 5) with increasing Rayleigh number were published in the last decade by the same group of researchers using mostly a fourth order finite volume scheme [18–22]. The square cavity remains a rather rarely tackled case in the literature because of its additional computational cost associated with the higher Rayleigh numbers for the transition to turbulence to occur compared with tall cavities. The combination of these aspects makes the simulation of square cavities at Rayleigh number in the fully turbulent regime very difficult to achieve. Even nowadays, many publications on such configuration are limited to LES results [23–25] or two-dimensional DNS. Sergent et al. [26] used Chebyshev collocation to carry out DNS of a fully three-dimensional box of square cross section with no slip walls on each of the six faces with aspect ratio 0.2 for the depth of the cavity. Puragliesi and Leriche [27] studied the flow in differentially heated cubic cavity at Rayleigh number of 10^9. To the authors' knowledge, this is the highest Rayleigh number ever considered for a true three-dimensional Direct Numerical Simulation for a differentially heated cavity of unit aspect ratio.

From an engineering standpoint, Computational Fluid Dynamics approaches relying on Reynolds Averaged Navier Stokes (RANS) equations are normally used. Application of standard turbulence models such as the $k-\varepsilon$ model associated with standard wall functions was made in differentially heated cavity some time ago [28]. However, numerous studies over the years have shown that application of turbulence models that were initially developed for forced convection flows is inappropriate due to the specific aspects of buoyancy driven flows such as the coexistence of laminar and turbulent regions and the presence of large scale structures. A review of the limitations of single-point mathematical closure when simulating buoyancy driven flow was carried out by Hanjalic [29]. The recent developments of second-moment closure approaches [30–32] focusing on buoyancy driven flows still relies heavily on very simple configurations such as mixed convection in a channel and vertical differentially heated channels [33–35], where the very important turbulent budget data are available at only fairly low Rayleigh number. Very few examples of turbulent budget calculations are presented in publications dealing with the more complicated case of rectangular differentially heated cavities. To the authors' knowledge, Barhaghi and Davidson [36] are the only ones to present the full budgets using LES, making the results only qualitative as mentioned by the authors themselves.

In the present paper, Direct Numerical Simulation results for a Prandtl number equal to 0.71 and Rayleigh numbers varying between 10^8 and 10^{11} in a differentially heated square cavity with prescribed temperature on the horizontal walls are presented. In addition to the first and second order statistical moments, the full budgets of each component of the Reynolds stress tensor are presented as well as the budgets of the turbulent heat fluxes and temperature variance. The decision to focus on the square configuration was motivated by the fact that historically the application of classic turbulence models to this configuration resulted in the largest degree of discrepancy with experiments. In such configuration the two vertical buoyant boundary layers do not interact with each other as they can do in taller cavities via shear in the core of the domain, which makes its modelling more challenging for single point closure turbulence models. Unlike the more recent literature on the topic [37–39] that tends to focus on the coupling between conduction through the walls of the cavities, radiative effects and even particle transport in the fluid, at fairly low Rayleigh numbers, the present work focuses on reaching high Rayleigh numbers to provide important insights from a turbulence modelling standpoint. The analysis presented herein focuses on data of relevance to the RANS modelling framework and does not provide a quantitative analysis of low frequency unsteadiness inherent to such flows. Despite a significant dwindling of academic research focusing on RANS models in aid of LES or hybrid approaches, these models will remain the industry standard for the foreseeable future. It is therefore very important to provide accurate data relevant to this modelling framework that can be used to validate and improve the latest developments in field (see [40,31,41] for instance). The data presented herein and available on the ERCOFTAC classic database are therefore expected to be a valuable resource for the turbulence modeling community as such data are very scarce for buoyancy driven flow configurations other than the simple vertical differentially heated channel.

The paper is organised as follows. In Section 2, the computational methodology will be presented as well as the flow configurations. Then, in Section 3, the influence of the Rayleigh number on the flow with a prescribed linear temperature variation on the horizontal wall is investigated. The latter includes comparison of first order moments with scaling laws, analysis of the evolution

of the Nusselt number and level of thermal stratification together with a detailed examination of each component of the Reynolds stresses, turbulent heat fluxes and temperature variance budgets of the buoyant boundary layer in the vicinity of the hot wall.

2. The computational method

2.1. Computational domain and governing equations

In the present paper a three dimensional computational domain is considered for all the calculations, as illustrated in Fig. 1. The dimensions of the cavity in each direction are L_x, L_y and L_z. The paper being focused on square cavity flows, $L_x = L_y = H$ for all configurations. The focus is on the case where the flow is statistically two-dimensional so that periodic boundary condition can be applied in the z-direction of the domain. The depth of the cavity is adjusted to minimize the computational cost of the simulation at a given Rayleigh number whilst ensuring that the turbulence correlation length in the z-direction is shorter than half of the cavity depth. This corresponds to a cavity infinitely long in the z-direction. The cavity is filled with an incompressible Newtonian fluid of thermal diffusivity α, kinematic viscosity ν and thermal expansion coefficient β. To account for the variation of density with temperature, the Boussinesq approximation is invoked. The effect of radiation is not considered in the present simulations.

The governing equations can be written in the following form using Cartesian tensor notations and the skew-symmetric form of the momentum equations solved:

$$\frac{\partial u_j}{\partial x_j} = 0 \tag{1}$$

$$\frac{\partial u_i}{\partial t} + \frac{1}{2}\left(\frac{\partial u_i u_j}{\partial x_j} + u_j \frac{\partial u_i}{\partial x_j}\right) = -\frac{\partial p}{\partial x_i} + Pr\, Ra^{-1/2} \frac{\partial^2 u_i}{\partial x_j \partial x_j} - Pr\, \theta \frac{g_i}{g} \tag{2}$$

$$\frac{\partial \theta}{\partial t} + u_j \frac{\partial \theta}{\partial x_j} = Ra^{-1/2} \frac{\partial^2 \theta}{\partial x_j \partial x_j} \tag{3}$$

where $\boldsymbol{u} = (u_i, i \in [\![1,3]\!]), p, \theta, \boldsymbol{x}$ and t respectively denote the *normalised* velocity, piezometric pressure, temperature, position and time. The gravity vector is chosen such that $\boldsymbol{g}/g = (-1, 0, 0)$ with g denoting its magnitude. If the superscript * denotes the corresponding physical quantities, then the relationships between the physical and normalised quantities are as follows:

$$\boldsymbol{u}^\star = \frac{\alpha Ra^{1/2}}{H}\boldsymbol{u} \quad p^\star = \frac{\alpha^2 Ra}{H^2} p \quad \theta^\star = \theta \Delta\theta^\star + \theta^\star_{avg}$$
$$t^\star = \frac{H^2 Ra^{-1/2}}{\alpha} t \quad \boldsymbol{x}^\star = H\boldsymbol{x} \tag{4}$$

The fluid Prandtl number Pr is defined by ν/α and the Rayleigh number Ra by $\left(g\beta\Delta\theta^\star H^3\right)/(\nu\alpha)$. $\theta^\star_{avg}$ and $\Delta\theta^\star$ in Eq. (4) denote the average temperature in the cavity and the temperature difference applied between the walls respectively. In the remainder of the paper, the components of the position vector $\boldsymbol{x}$ will be denoted by (x, y, z) and unless index notations are used, the components of the velocity vector $\boldsymbol{u}$ will be denoted by (u, v, w) for simplicity.

As regards the boundary conditions, the wall at $y = 0$ and $y = 1$ are kept at a constant temperature $\theta = +0.5$ and $\theta = -0.5$, respectively, and have a no slip boundary condition $\boldsymbol{u} = 0$. The lower and upper walls of the cavity at $x = 0$ and $x = 1$ also have zero slip ($\boldsymbol{u} = 0$) for the velocity. As mentioned in the introduction, the simulations will represent a cavity with highly conductive horizontal walls, which corresponds to a linear temperature profile $\theta(y) = 0.5 - y$, applied as Dirichlet boundary condition. On the front and back of the cavity at $z = 0$ and $z = L_z/H$, periodic boundary conditions are applied.

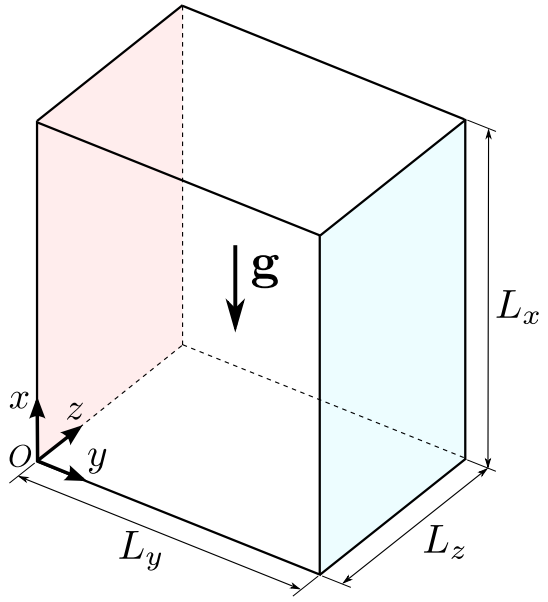

Fig. 1. Computational domain (not to scale) and coordinate system used in each directions.

2.2. Numerical scheme

In the present paper the governing equations presented in the previous section are solved using the open-source DNS code *incompact3d* developed by Laizet and Lamballais[42]. This code is optimised to maintain good scalability up to $O\left(10^5\right)$ computational cores [43]. The governing equations are discretised using a sixth order compact finite difference scheme [44]. The momentum equations are solved using a skew-symmetric form, which is known to minimize aliasing errors while remaining energy preserving [45]. The time advancement is made using a third-order Runge-Kutta scheme along with a three stage fractional step method. The Poisson equation arising for pressure at each substep to enforce continuity is solved with a direct method based on the concept of modified wavenumber in spectral space. In order to avoid spurious oscillations, a partially staggered arrangement for pressure and velocity nodes is used. For more details about the implementation of the numerical methods and the formulation of the streching function used to handle non-uniform meshes, the reader is referred to Laizet and Lamballais [42]. The code has been extensively validated over the last ten years for purely hydrodynamic, heat transfer [46] and buoyancy driven flow configurations [47]. Further validation of the code is carried out here for the specific case of a differentially heated cavity at $Ra = 2 \times 10^9$ in a 4:1 cavity with adiabatic horizontal walls and the results are compared against the DNS of Trias et al. [19] in appendix 1. The implementation of the data processing procedures to calculate the full turbulent budgets were extensively validated against reference channel flows DNS as presented in Sebilleau [41].

2.3. Statistical averaging of the data and domain dimensions

For each simulation, when possible, a snapshot of the flow obtained at a lower Rayleigh number was interpolated onto the mesh and used as initial condition. The flow was then developed in time until a statistically steady state was reached.

In the remainder of the paper, various statistically averaged results are presented. The averaging procedure is carried out in time and space in the homogeneous z- direction. The average of any quantity $\phi(\boldsymbol{x},t)$ is denoted by an overbar and is mathematically defined by:

$$\overline{\phi}(x,y) = \frac{1}{\Delta t_{avg}} \frac{1}{L_z} \int_z \int_t \phi(x,y,z,t) dt\, dz \tag{5}$$

The symmetry of the flow around the cavity centre $(x,y) = (0.5, 0.5)$ is also used to improve the convergence of the statistics for the budgets only. The corresponding fluctuating part of $\phi(\boldsymbol{x},t)$ is simply defined by $\phi'(\boldsymbol{x},t) = \phi(\boldsymbol{x},t) - \overline{\phi}(x,y)$. In order to make the notations simpler, the average velocity components and average temperature will be simply denoted by (U,V,W) and Θ.

Because of the very large number of derivatives to compute to obtain the full budgets, collecting statistics at every timestep was found to slow down the simulation by no less than an order of magnitude. The collection of statistical data in time was therefore effected every ten timesteps during the simulation. The convergence of the statistical data was ensured by examining the components of the budget of the $\overline{v'v'}$ Reynolds stress as the number of collected statistical samples increased. This component was found to be the slowest to converge and therefore provided the most conservative measure.

Another very important choice to make for each simulation is the domain dimension in the z-direction where the periodic boundary conditions are applied. For each simulation, the two-point correlation in space of all the velocity components and temperature was computed at several (x,y) positions in the cavity to ensure the turbulent field was uncorrelated at a separation of a half-period. The two-point correlation in space of a quantity $\phi(\boldsymbol{x},t)$ is defined by:

$$R_{\phi\phi}(x,y,r) = \frac{\overline{\phi'(x,y,z,t)\phi'(x,y,z+r,t)}}{\overline{\phi'(x,y,z,t)^2}} \tag{6}$$

Graphs showing appropriate decay of the two point correlation in the z-direction for each velocity component as well as for temperature are shown in Fig. 3 for each Rayleigh number simulated. In cases where multiple simulations were carried out at the same Rayleigh number, the two-point correlation is only shown for the largest domain.

A summary of all the simulations carried out in the present work is given in Table 1. The mesh was carefully chosen to ensure that all turbulent fluctuations down to the Kolmogorov scale are resolved. A grid dependence study is presented in appendix 2 at $Ra = 1.58 \times 10^9$ for a case detailed in Sebilleau [41] with a slightly different temperature profile on the horizontal walls. Similar refinement is then applied to cases with higher Rayleigh number. In addition to this, the computed gridspace to Kolmogorov length ratio $(\Delta x \Delta y \Delta z)^{1/3}/\eta$ (η denoting the Kolmogorov length scale) is given in Fig. 2 to show that all dissipative scales are properly resolved for each Rayleigh number. The time-step is chosen such that it remains within the stability limits of the fully explicit time-advancement, which can become particularly computationally expensive because of the limit imposed by the viscous terms. The satisfaction of the latter is also sufficient to resolve accurately all the turbulent time scales.

3. Results and discussion

In the present section, the aforementioned simulations based on a linear temperature profile applied on the top and bottom walls are considered in order to study the influence of the Rayleigh number. This boundary condition was chosen in place of the more classic adiabatic boundary conditions because, in the present square cavity configuration, adiabatic conditions yield an almost entirely laminar cavity with only small turbulent regions at the top left and bottom right corners. With this boundary condition, the achieved turbulence levels are higher at equivalent Rayleigh number than the adiabatic counterpart which helped reaching unprecedented turbulence levels for such flow. This point is very important as most of the available DNS data on buoyancy driven flows suffer from low-Re effects that affect turbulence modelling.

3.1. Nusselt number prediction

From an engineering perspective, the mean Nusselt number on the vertical walls, which represents the global heat transfer

Table 1
Summary of all the simulations presented in the present paper. Δt_{dev} indicate the simulation time before the beginning of the averaging procedure. The time indicated is from a uniform $\Theta = 0$ initial condition for DNS1. For all other simulation (DNS2 to DNS4), it represents the simulation time starting from an interpolation of a snapshot of the previous simulation onto the new mesh. β_s refers to the parameter β for the stretching function defined in equation (53) of Laizet and Lamballais [42].

Simulation	Ra	Pr	L_z/H	$N_x \times N_y \times N_z$	β_s	Δt	Horizontal BC	Δt_{dev}	Δt_{avg}
DNS1	1.0×10^8	0.71	1.0	$513 \times 257 \times 128$	0.09	7×10^{-4}	linear	200	350
DNS2	1.58×10^9	0.71	0.4	$1025 \times 513 \times 128$	0.1	7×10^{-4}	linear	50	150
DNS3	1.0×10^{10}	0.71	0.3	$2049 \times 1025 \times 128$	0.09	3×10^{-4}	linear	50	120
DNS4	1.0×10^{11}	0.71	0.15	$2593 \times 1459 \times 192$	0.05	2×10^{-4}	linear	25	55

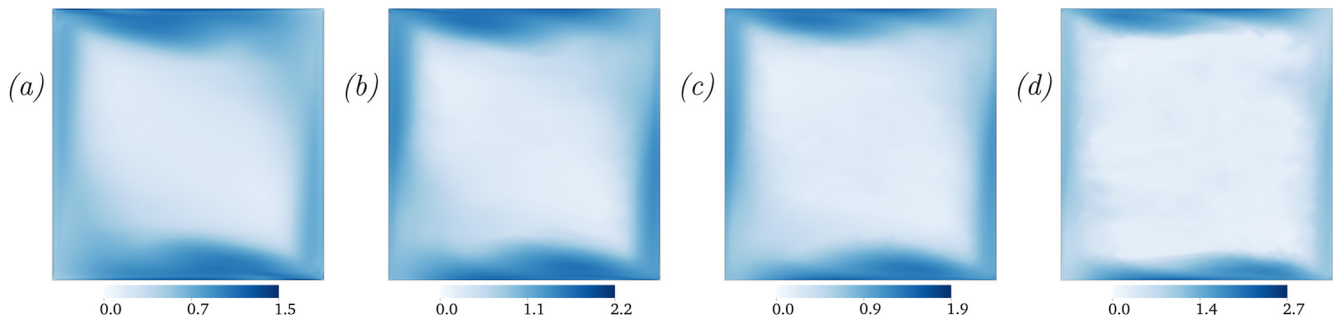

Fig. 2. Computed grid to Kolmogorov length scale ratio $(\Delta x \Delta y \Delta z)^{1/3}/\eta$ (a)$Ra = 1.0 \times 10^8$(b) $Ra = 1.58 \times 10^9$(c) $Ra = 1.0 \times 10^{10}$ (d) $Ra = 1.0 \times 10^{11}$.

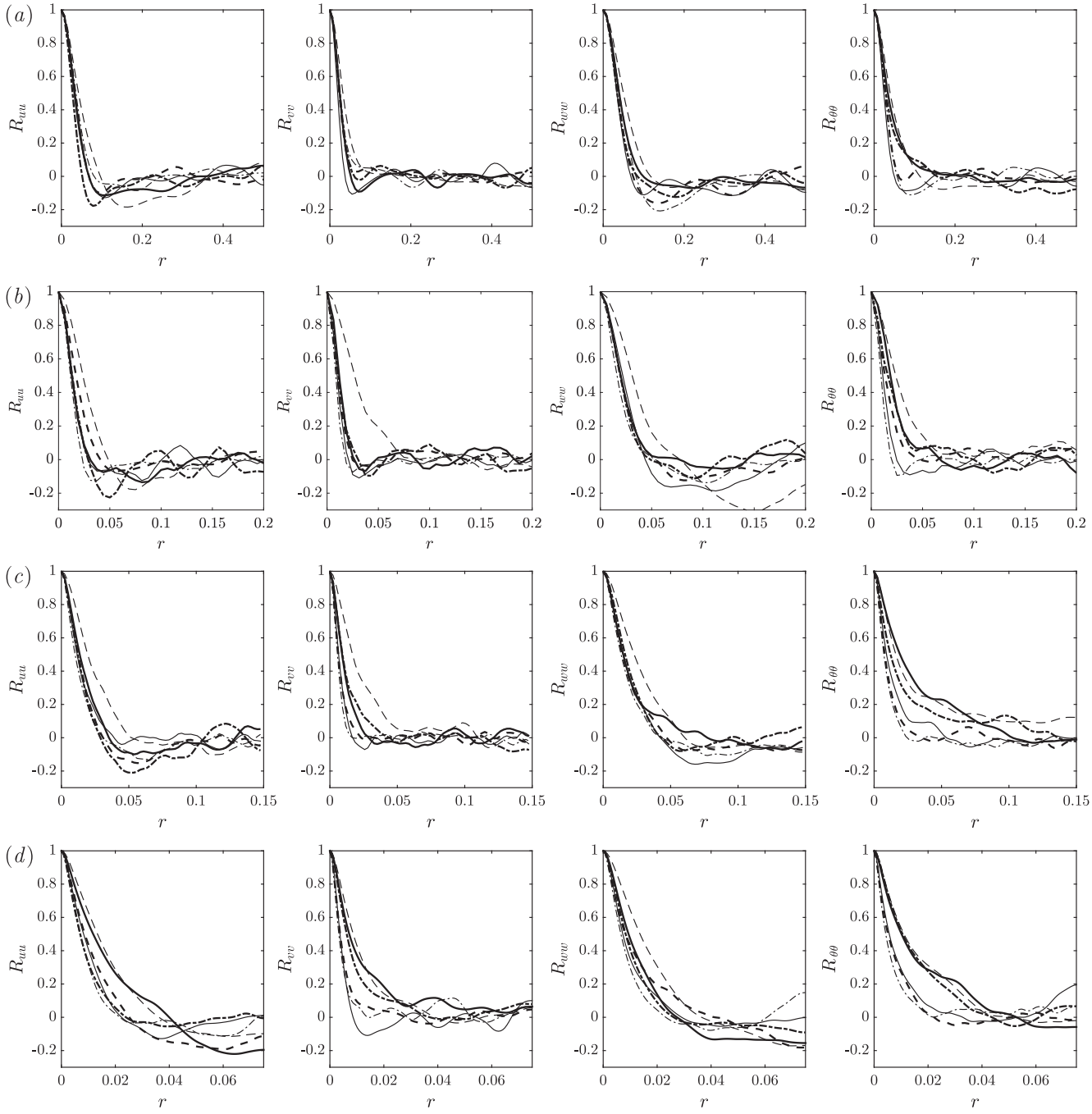

Fig. 3. Two point correlation in the z-direction for several (x, y) positions in the cavity and different Rayleigh number: (a) $Ra = 10^8$; (b) $Ra = 1.58 \times 10^9$ (c) 10^{10} (d) 10^{11} (——— $(x,y) = (0.2, 0.01)$ — — — $(x,y) = (0.2, 0.05)$ — · — $(x,y) = (0.5, 0.01)$ ——— $(x,y) = (0.5, 0.05)$ — — — $(x,y) = (0.8, 0.01)$ — · — $(x,y) = (0.8, 0.05)$).

Table 2
Summary of some integral quantities obtained for each simulation.

Simulation	DNS1	DNS2	DNS3	DNS4
Ra	1×10^8	1.58×10^9	1.0×10^{10}	1.0×10^{11}
$\langle Nu_{\text{hot}} \rangle$	25.3	61.1	110.6	230.7
$\langle Nu_{\text{cold}} \rangle$	25.3	60.8	111.5	231.6
$\langle Nu_{\text{bottom}} \rangle$	12.8	26.3	41.6	85.1
$\langle Nu_{\text{top}} \rangle$	12.8	26.3	42.1	84.4
$\langle S_\theta \rangle$	0.42	0.49	0.41	0.36

coefficient between the hot and cold wall of the cavity, is important. The computed mean Nusselt number on each of the walls of the cavity are summarised in Table 2 and are defined as follows:

$$\langle Nu_{\text{hot}} \rangle = -\int_0^1 \frac{\partial \Theta}{\partial y}(x,0)dx, \quad \langle Nu_{\text{cold}} \rangle = -\int_0^1 \frac{\partial \Theta}{\partial y}(x,1)dx \tag{7}$$

$$\langle Nu_{\text{bottom}} \rangle = -\int_0^1 \frac{\partial \Theta}{\partial x}(0,y)dy, \quad \langle Nu_{\text{top}} \rangle = -\int_0^1 \frac{\partial \Theta}{\partial x}(1,y)dy \tag{8}$$

A very large body of work has focused in the past establishing correlations giving the mean Nusselt number as a function of the Rayleigh and Prandtl number for Rayleigh-Benard convection. However, as mentioned by Trias et al. [20], the case of laterally heated cavities has attracted much less attention from the scientific community. In the case of a vertical buoyant boundary layer, there are two limiting cases for Nusselt correlations: $Nu \sim Ra^{1/4}$ for the laminar case and $Nu \sim Ra^{1/3}$ for the fully turbulent case.

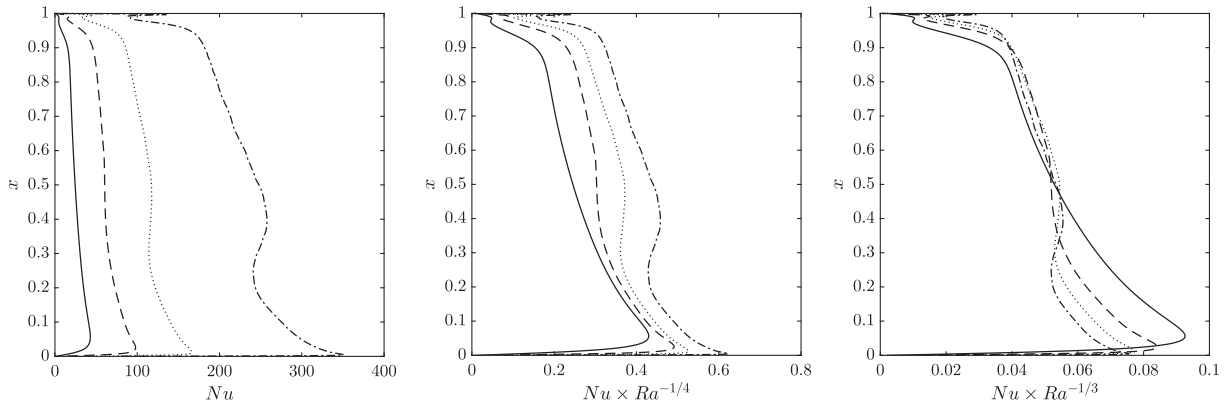

Fig. 4. Comparison of the Nusselt number distribution along the cavity hot wall with different scaling: ——— $Ra = 10^8$ — — — $Ra = 1.58 \times 10^9$ - - - - - $Ra = 10^{10}$ — - — $Ra = 10^{11}$.

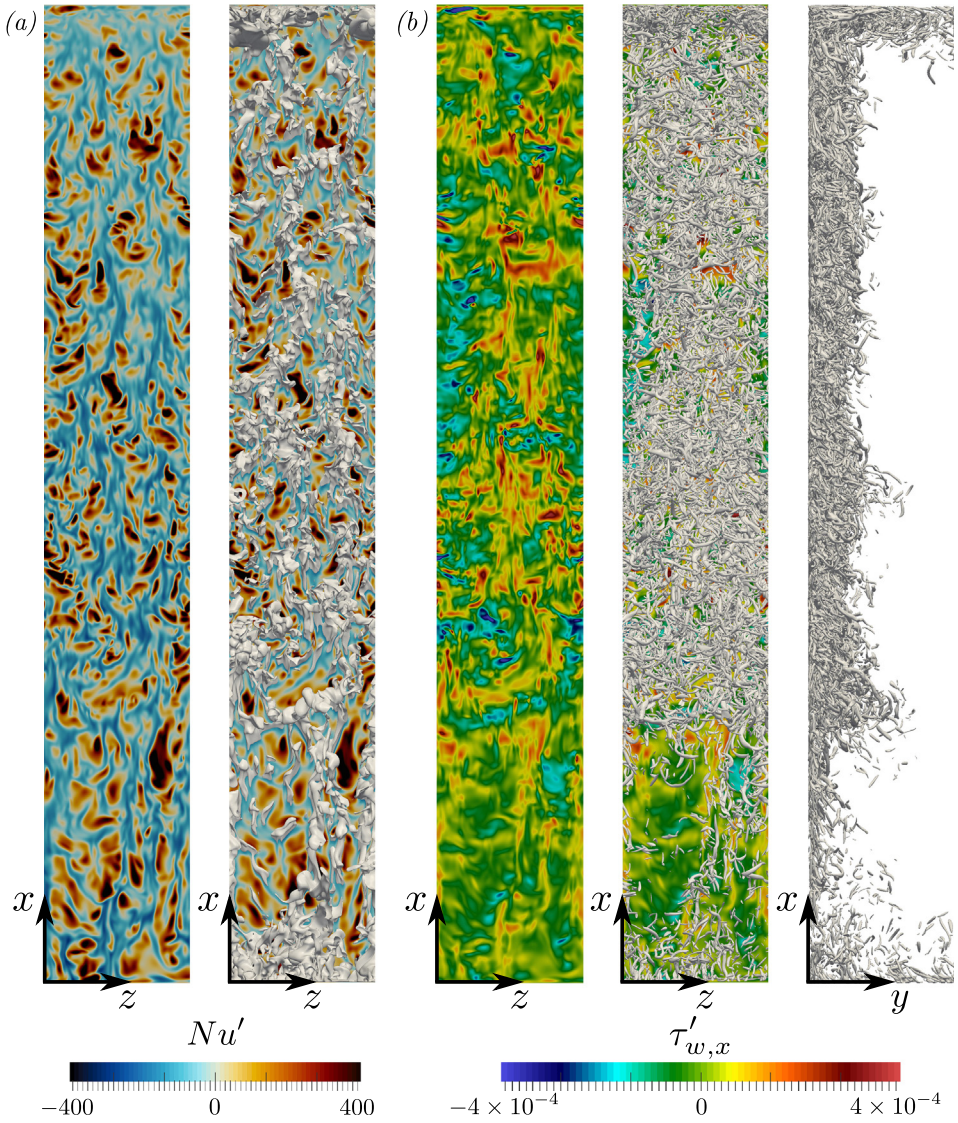

Fig. 5. Visualisation of the turbulent flow structures in the vicinity of the cavity vertical hot wall at $Ra = 10^{11}$: (a) Scalar contour of instantaneous Nusselt number fluctuation Nu' with iso-temperature fluctuation $\theta' = 0.07$ is shown in grey; (b) Scalar contour of instantaneous streamwise wall shear stress fluctuation $\tau'_{w,x}$ and iso-surface $Q = 150$ in grey. (The colorbar scales are saturated and symmetric around zero for visualisation purposes). (For interpretation of the references to colour in this figure legend, the reader is referred to the web version of this article.)

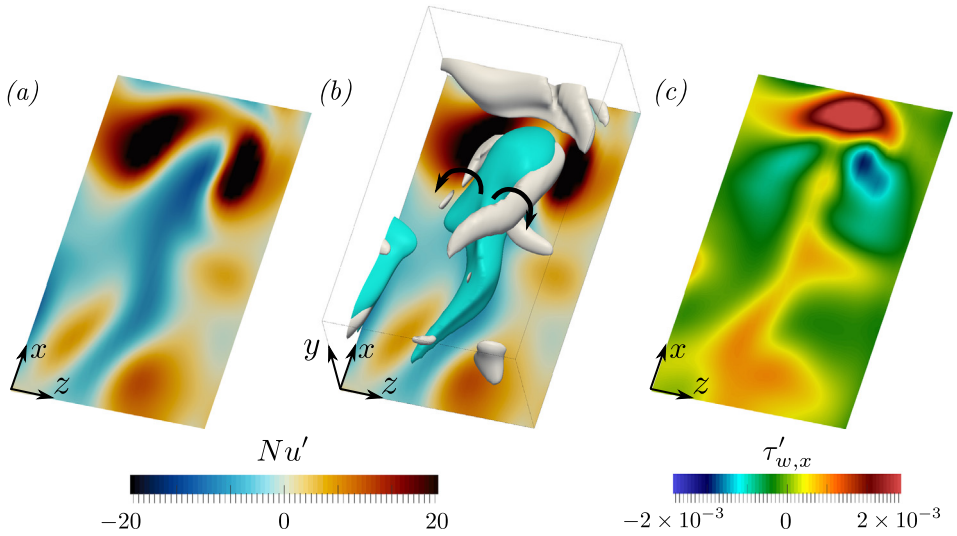

Fig. 6. Characteristic flow structures arising from the ejection of a buoyant plume from the lower horizontal wall of the cavity rising along vertical hot wall of the cavity for the case at $Ra = 10^8$: (a) Instantaneous Nusselt number fluctuations Nu'; (b) Instantaneous Nusselt number fluctuations with isosurface of Q = 8 (in grey) and iso-temperature fluctuation $\theta' = 0.05$ (in blue); (c) Contour of streamwise wall shear stress fluctuation on the hot wall τ'_{wx} (The colorbar scales are saturated and symmetric around zero for visualisation purposes). (For interpretation of the references to colour in this figure legend, the reader is referred to the web version of this article.)

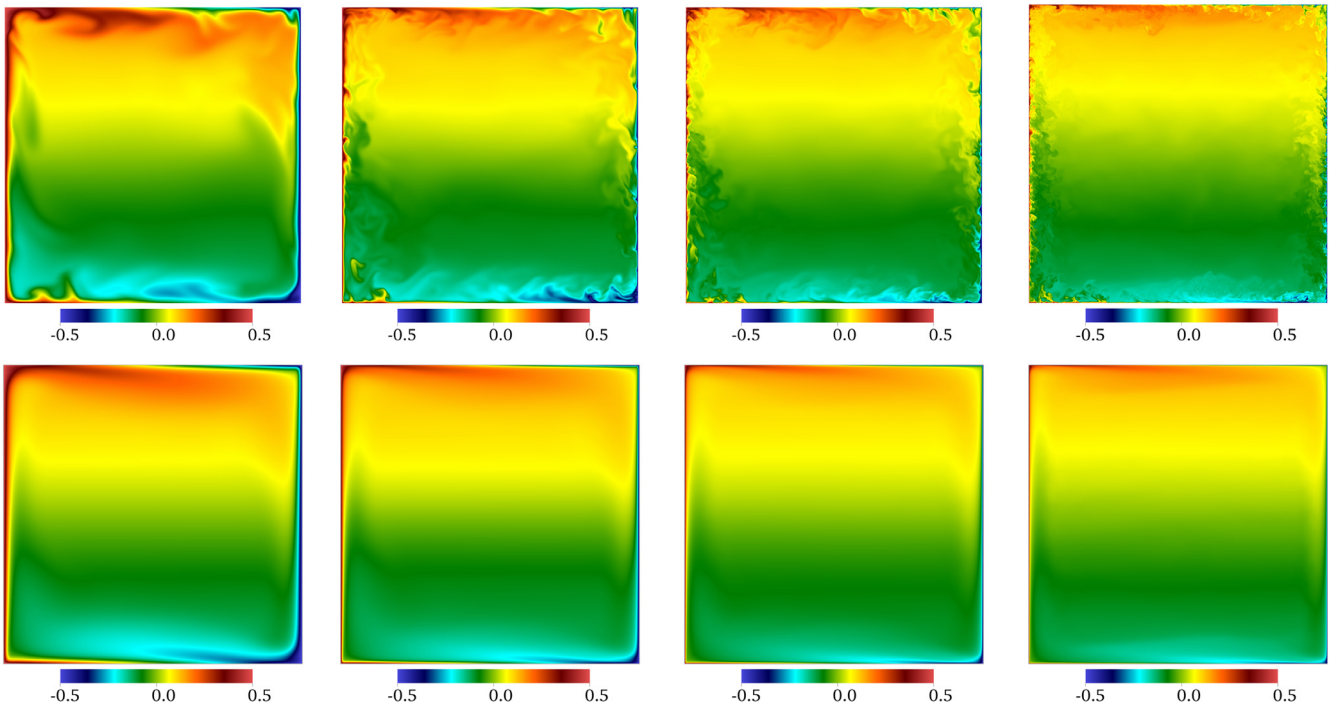

Fig. 7. From left to right: DNS1, DNS2, DNS3 and DNS4. On the top row, instantaneous temperature distribution $\theta(x, y, Lz/2, t)$. On the bottom row, average temperature distribution $\Theta(x, y)$.

In the present case, a least square regression gives $Nu = 0.0691Ra^{0.3203}$. The latter is in very close agreement with the aforementioned *one-third* power law for fully turbulent vertical buoyant boundary layers. In comparison, Trias et al. [20] obtained $Nu = 0.182Ra^{0.275}$ for differentially heated cavity of aspect ratio 4 and adiabatic horizontal walls. In their configuration most of the vertical boundary layer remained laminar, which explains the power law exponent being closer to the *one-fourth* laminar law.

The mean Nusselt number profiles along the hot wall of the cavity are presented in Fig. 4. It can be observed that in the lower part of the cavity ($x < 0.3$), the profiles tend to follow a $Ra^{1/4}$ scaling whereas in the upper part they tend to follow the fully turbulent $Ra^{1/3}$ scaling law. The correlation is also in very good agreement with Yu et al. [48] in a square cavity with adiabatic horizontal boundary conditions for Rayleigh numbers between 10^3 and 10^7. Yu et al. [48] obtained $Nu = 0.13Ra^{0.31}$ and conjectured that the power law exponent obtained is independent of the flow regime (laminar or turbulent). The presence of thermal stratification in the core and thin buoyant boundary layers near the wall are supposedly sufficient to obtain a near *one-third* scaling law also

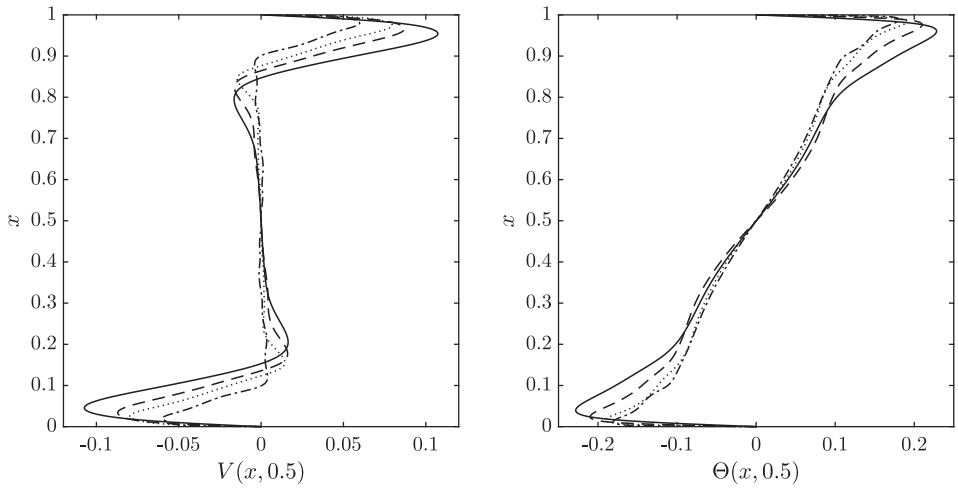

Fig. 8. Comparison of mean velocity at different cavity height : ——— $Ra = 10^8$ — — — $Ra = 1.58 \times 10^9$ - - - - - $Ra = 10^{10}$ — - — $Ra = 10^{11}$.

obtained in Rayleigh–Benard convection and other natural convection systems. The present results tend to agree with this hypothesis.

3.2. Coherent flow structures

The present flow pattern is characterised by vertical thermal stratification in the core where the flow remains almost quiescent with four boundary layers near the walls. The main difference between the present and the more common configuration (with horizontal adiabatic walls) is the presence of unstable density gradients in the vicinity of the horizontal walls in the bottom left and top right corners of the cavity. The latter triggers the ejection of buoyant plumes transported toward the vertical walls by clockwise circulation in the cavity. These plumes, clearly visible in the top panels of Fig. 7 for all the Rayleigh numbers considered, are the reason why the transition to turbulence occurs at a lower Rayleigh number than in the adiabatic case. They also enhance the level of turbulence by destabilising the vertical buoyant boundary layers. Whereas in an adiabatic case a clear transition from laminar to turbulence would occur along the vertical wall, in the present case, turbulent structures can be observed along the entire vertical wall as illustrated in Fig. 5b. Moreover, a clear thickening of the turbulent region can be observed in the last panel in Fig. 5 around $x \sim 0.35$. This thickening of the turbulent region is associated with turbulence enhancement that corresponds to the local maxima in Nusselt number observed in Fig. 4 around the same x-position along the hot wall. As the Rayleigh number is increased the location of turbulence enhancement moves closer to the bottom wall. The scalar contour of instantaneous Nusselt number fluctuation in Fig. 5a and iso-temperature fluctuation contour show elongated structures along the vertical x-direction. These structures correspond to hot buoyant plumes ejected from the horizontal walls rising along the vertical wall. Such structures are still noticeable in the upper part of the hot wall where the level of turbulence is much higher. They are associated to streaks of negative Nusselt number fluctuation and positive streamwise wall shear stress fluctuation. This is shown in Fig. 5 for the highest Rayleigh number but are present for all the simulated Rayleigh numbers. A focus on a buoyant hot plume is shown in Fig. 6 for the case at $Ra = 10^8$. The iso-temperature fluctuation contours shown in blue represents the envelope of the buoyant plume surrounded by two counter-rotating vortices (in grey with arrows indicating the rotation of the vortices). These counter-rotating vortices are bringing colder fluid from the core towards the hot wall, which increases the temperature gradient and therefore explains the locally high positive Nusselt fluctuation observed underneath. These structures are clearly visible at $Ra = 10^8$ as there is almost no turbulence in the outer region of the boundary layer at such Rayleigh number. However, similar structures can still be observed in the high Rayleigh number cases.

3.3. First and second order statistics

The first aspect, which is characteristic of cavity configurations, is the formation of a thermal stratification in the core of the cavity as illustrated and discussed qualitatively in the previous section. Fig. 8 gives the horizontal velocity and temperature distribution at the cavity midwidth for the four values of Rayleigh number considered. As the Rayleigh number is increased, the velocity boundary layers along the horizontal cavity walls become thinner and the proportion of the core region where the velocity tends to zero increases. The variations of the level of thermal stratification can be quantified using the mean stratification parameter denoted $\langle S_\Theta \rangle$ and defined by:

$$\langle S_\Theta \rangle = \frac{\partial \Theta}{\partial x}(0.5, 0.5) \tag{9}$$

The computed values of the mean stratification parameter are summarised in Table 2. The stratification parameter tends to decrease when the Rayleigh number is increased, with the exception of the case at $Ra = 10^8$ where the level of turbulence is extremely low. An opposite trend was observed by Trias et al. [20,21] in a 4:1 tall cavity with adiabatic horizontal walls. They conjectured that the variation of $\langle S_\Theta \rangle$ is related to the upstream displacement of the position of transition to turbulence in the vertical boundary layers. Analysis of the data from the same authors shows that even at their highest Rayleigh number the two vertical boundary layers are laminar at the cavity midheight, where the mean stratification parameter is calculated. In the case of a square cavity, for the three largest Rayleigh number both vertical boundary layers are turbulent at the cavity midheight. This difference could explain the opposite trends and it would be interesting to see the evolution of the stratification at higher Rayleigh number in this 4:1 cavity.

Vertical buoyant boundary layers have attracted much less attention than forced convection boundary layers or even horizontal buoyant boundary layers in a Rayleigh Bénard convection configurations. The experimental work from Tsuji and Nagano [49,50] measuring first and second order moments in a vertical buoyant boundary layer in the vicinity of a hot plate in a quiescent

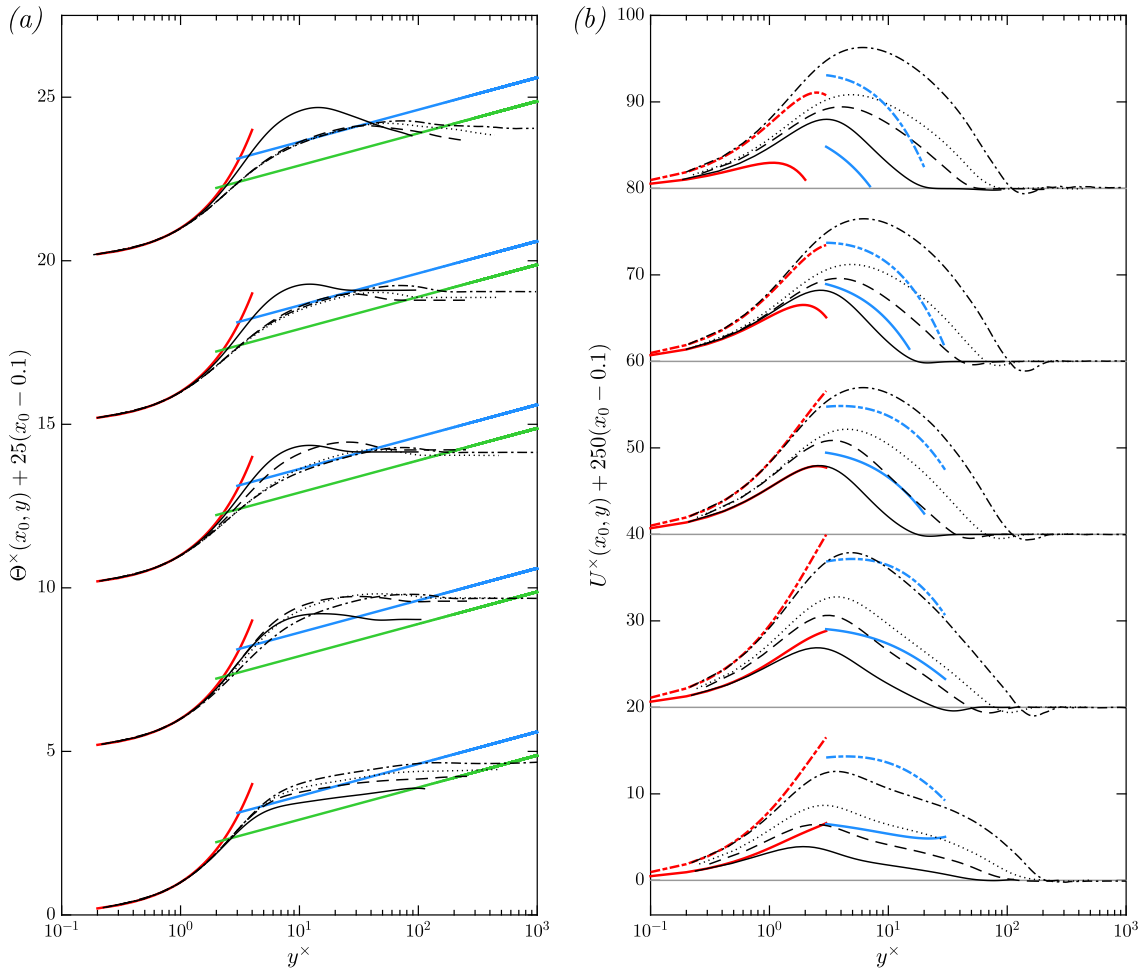

Fig. 9. Comparison of first order moments with scaling laws from [52] at different cavity heights ($x_0 = 0.1 - 0.3 - 0.5 - 0.7 - 0.9$): (a) Temperature $\Theta^\times$ ($\Theta^\times = y^\times$ $\Theta^\times = 0.427\ln(y^\times)+1.93$ $\Theta^\times = 0.427\ln(y^\times)+2.65$) (b) Velocity $U^\times$ ($U^\times = \frac{\partial U^\times}{\partial y^\times}|_w y^\times - \frac{1}{2}\Theta_0 y^{\times 2} + \frac{1}{6}y^{\times 3}$ $U^\times = \frac{CPr}{\sigma_t} y^\times (C[\ln(y^\times)-2]+D-\Theta_0^\times)+E\ln(y^\times)+F$) ($Ra = 10^8$ $Ra = 1.58\times10^9$ $Ra = 10^{10}$ $Ra = 10^{11}$).

Table 3
Summary of normalisation factors used to convert quantities normalised by Eq. (4) into classic wall units. All the wall derivatives are computed locally and **not** averaged over the entire wall.

Quantity to normalise	Normalisation factor
Distance y	$Ra^{1/4}Pr^{-1/2}\frac{\partial U}{\partial y}\Big\vert_w^{1/2}$
Velocity $\boldsymbol{u}$	$Ra^{1/4}Pr^{-1/2}\frac{\partial U}{\partial y}\Big\vert_w^{-1/2}$
Temperature θ	$Ra^{1/4}Pr^{1/2}\frac{\partial U}{\partial y}\Big\vert_w^{1/2}\frac{\partial \Theta}{\partial y}\Big\vert_w^{-1}$
Terms in budget of $\overline{u_i'u_j'}$	$Ra^{1/2}Pr^{-1}\frac{\partial U}{\partial y}\Big\vert_w^{-2}$
Terms in budget of $\overline{u_i'\theta'}$	$Ra^{1/2}\frac{\partial U}{\partial y}\Big\vert_w^{-1}\frac{\partial \Theta}{\partial y}\Big\vert_w^{-1}$
Terms in budget of $\overline{\theta'\theta'}$	$Ra^{1/2}Pr\frac{\partial \Theta}{\partial y}\Big\vert_w^{-2}$

environment remains a reference nowadays. Contrary to forced convection boundary layers where the existence of a logarithmic law of the wall is widely accepted, in buoyant boundary layers, consistent scaling laws over a wide range of configurations do not seem to exist. The temperature profiles expressed in viscous wall units do exhibit a near wall region where the relationship $\Theta^+ = Pr\, y^+$ is valid. This region extends up to 5 wall units approximately, which is similar to the forced convection case. However, as shown by [49], the validity of the linear profile $U^+ = y^+$ in the near wall region does not extend beyond $y^+ = 1$. Since then, various attempts have been made to obtain inner and outer scaling laws for velocity and temperature. The work of George and Capp [51], based on a two-layer approach and dimensional analysis of a vertical buoyant boundary layer, obtained a one third power law for temperature in a vertical buoyant boundary layer, which was later observed in the DNS profiles of Versteegh and Nieuwstadt [33]. However, the one third power law proposed by the same authors for the velocity was not found to hold. More recently Holling and Herwig [52] adopted a new approach based on the use of a single gradient diffusion hypothesis to model the Reynolds shear stress in the mean momentum equation. With such approximation, they were able to integrate the latter and propose an outer scaling law for velocity profiles. The scaling was selected here for comparison with the simulations as it represents one of the only work based on multiple experiments including the buoyant boundary layer of Tsuji and Nagano [49], the tall cavity measurement of Betts and Bokhari [53], and the square cavity from Ampofo and Karayiannis [17]. Holling and Herwig [52] obtained the following inner and outer scaling law for temperature (* denotes dimensioned quantities to remain consistent with the notations introduced in Eq. (4)):

$$\Theta^\times_{inner} = y^\times \qquad \text{and} \qquad \Theta^\times_{outer} = C\ln(y^\times) + D \tag{10}$$

where

$$y^\times = \frac{y^\star}{l^\star_{ref}} \qquad \Theta^\times = \frac{T^\star}{T^\star_{ref}} \tag{11}$$

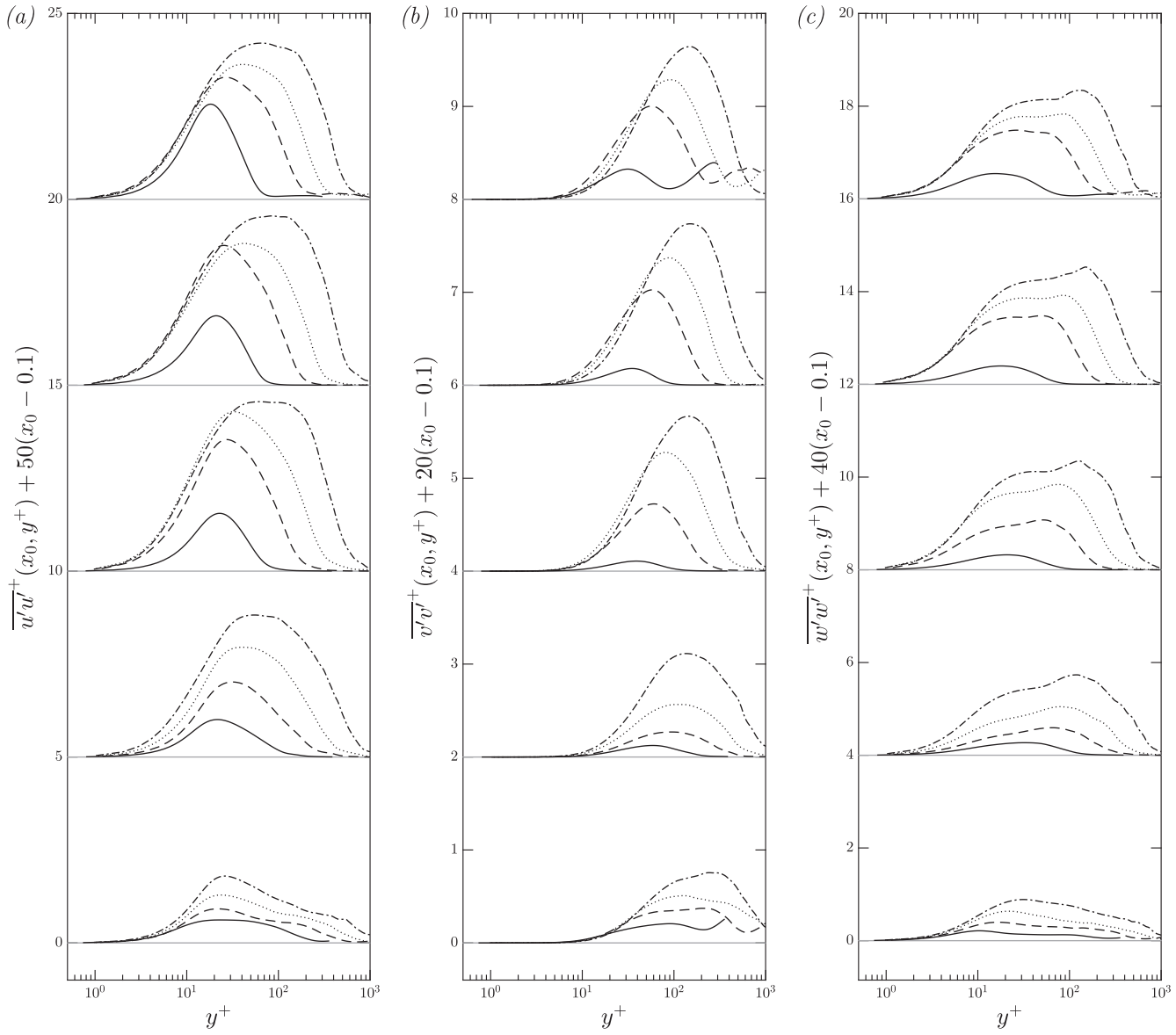

Fig. 10. Comparison of diagonal terms of the Reynolds stress tensor at different cavity heights ($x_0 = 0.1 - 0.3 - 0.5 - 0.7 - 0.9$) (——— $Ra = 10^8$ — — — $Ra = 1.58 \times 10^9$ - - - - - $Ra = 10^{10}$ — - — $Ra = 10^{11}$) : (a) $\overline{u'u'}$ (b) $\overline{v'v'}$ (c) $\overline{w'w'}$.

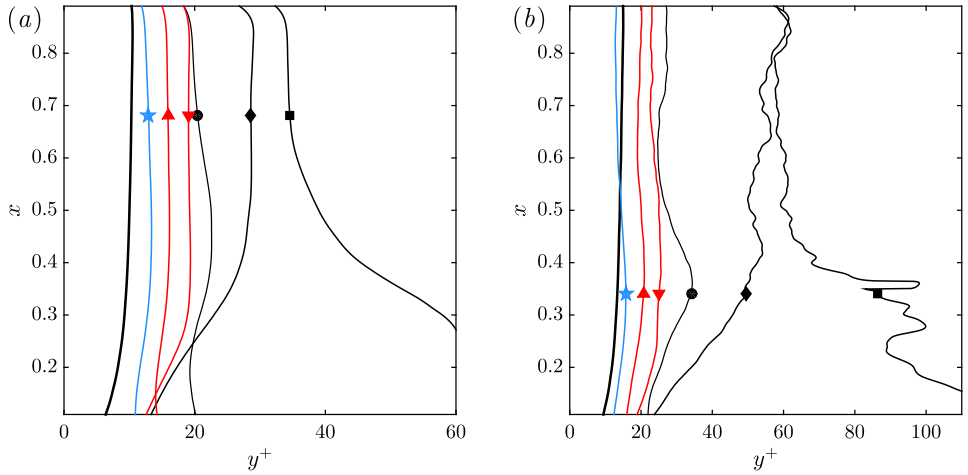

Fig. 11. Comparison of the position of the extrema of velocity, Reynolds stress, turbulent heat flux and temperature variance along the vertical buoyant boundary layer along the cavity hot wall (——— U_{max} • $\overline{u'u'}_{max}$ ■ $\overline{v'v'}_{max}$ ◆ $\overline{u'v'}_{max}$ ▲ $\overline{u'\theta'}_{max}$ ▼ $\overline{v'\theta'}_{max}$ ★ $\overline{\theta'\theta'}_{max}$): (a) $Ra = 10^8$ (b) $Ra = 1.58 \times 10^9$.

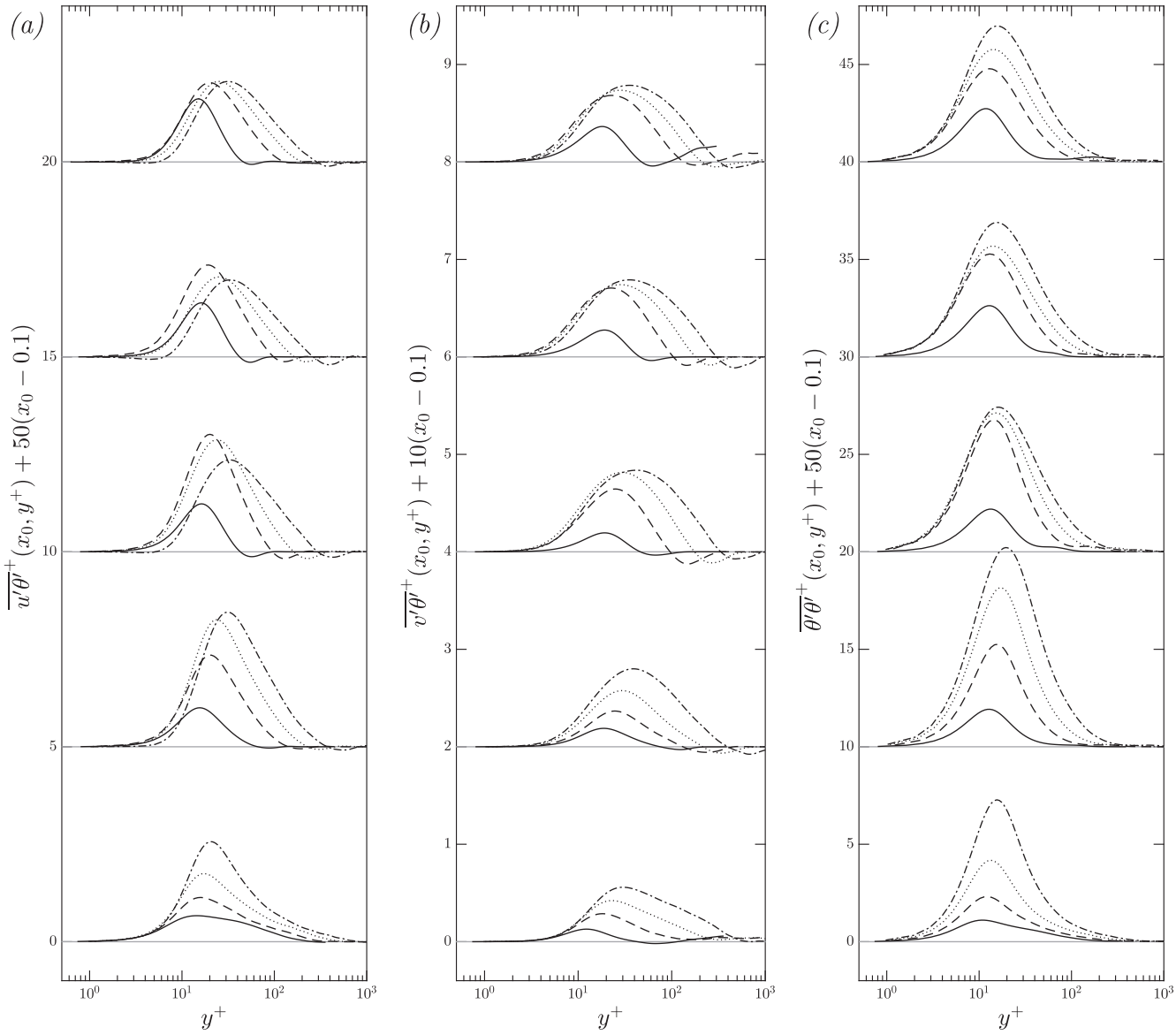

Fig. 12. Comparison of second order moments at different cavity heights ($x_0 = 0.1 - 0.3 - 0.5 - 0.7 - 0.9$) (——— $Ra = 10^8$ — — — $Ra = 1.58 \times 10^9$ - - - - - $Ra = 10^{10}$ — · — $Ra = 10^{11}$): (a) $\overline{u'\theta'}^{+}$ (b) $\overline{v'\theta'}^{+}$ (c) $\overline{\theta'\theta'}^{+}$.

and

$$T^{\star}_{ref} = \left(\frac{\alpha^2}{g\beta} \times \left|\frac{\partial T^{\star}}{\partial y^{\star}}\right|_w^3\right)^{1/4} \qquad l^{\star}_{ref} = \frac{T^{\star}_{ref}}{|\partial T^{\star}/\partial y^{\star}|_w} \tag{12}$$

They calibrated the coefficients of the outer law using the DNS data from [34] and suggested values of $C = 0.427$ and $D = 1.93$. The profiles obtained are plotted in Fig. 9a and compared with the inner and outer scaling laws given in Eq. (10). The linear relationship for the inner region exists for $y^{\times} < 2$ approximately. A log region develops in the outer layer in the upper part of the cavity for higher Rayleigh numbers. The coefficient $D = 1.93$ seems inappropriate in the present configuration and a corrected value of 2.65 appears to give a much better agreement. When [52] compared their scaling laws with the experimental data of [17] they observed worse discrepancy among all the aforementioned experimental and numerical database considered. The present comparison seems to agree with their observation.

As regard the velocity profiles, the following inner and outer scaling laws were derived by the same authors:

$$U^{\times}_{inner} = \left.\frac{\partial U^{\times}}{\partial y^{\times}}\right|_w y^{\times} - \frac{1}{2}\Theta_0 y^{\times 2} + \frac{1}{6} y^{\times 3} \tag{13}$$

$$U^{\times}_{outer} = \frac{CPr}{\sigma_t} y^{\times}(C[\ln(y^{\times}) - 2] + D - \Theta_0) + E\ln(y^{\times}) + F \tag{14}$$

where

$$U^{\times} = \frac{u^{\star}}{U^{\star}_{ref}} \qquad \text{with} \qquad U^{\star}_{ref} = \frac{g\beta T^{\star 3}_{ref}}{\nu} \times \left|\frac{\partial T^{\star}}{\partial y^{\star}}\right|_w^{-2} \tag{15}$$

and:

$$\Theta_0 = (T^{\star}_w - T^{\star}_0)/T^{\star}_{ref} \qquad E = 0.49\left.\frac{\partial U^{\times}}{\partial y^{\times}}\right|_w - 2.27$$

$$F = 1.28\left.\frac{\partial U^{\times}}{\partial y^{\times}}\right|_w + 1.28 \tag{16}$$

σ_t denotes a turbulent Prandtl number chosen equal to 0.9

Comparison between the present computations and the velocity scaling laws is given in Fig. 9b. The inner velocity scaling is in good

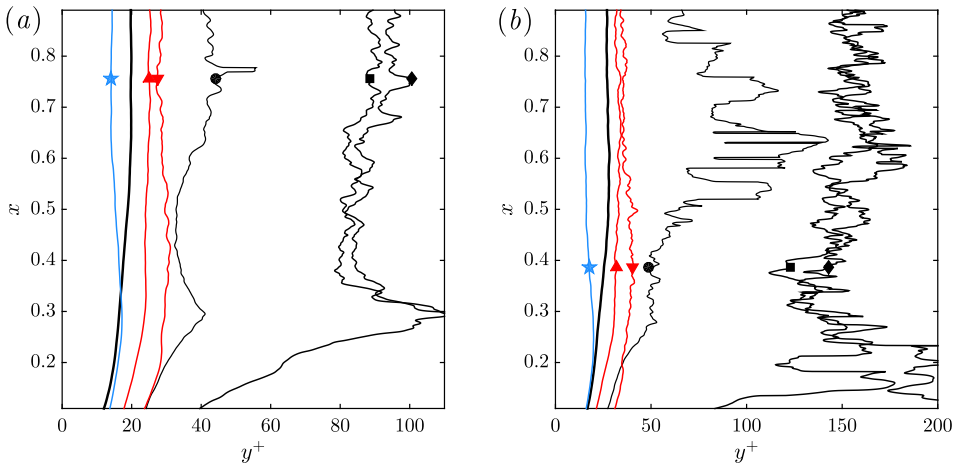

Fig. 13. Comparison of the position of the extrema of velocity, Reynolds stress, turbulent heat flux and temperature variance along the vertical buoyant boundary layer along the cavity hot wall (U_{max} • $\overline{u'u'}_{max}$ ■ $\overline{v'v'}_{max}$ ◆ $\overline{u'v'}_{max}$ ▲ $\overline{u'\theta'}_{max}$ ▲ $\overline{v'\theta'}_{max}$ ★ $\overline{\theta'\theta'}_{max}$): (a) $Ra = 10^{10}$ (b) $Ra = 10^{11}$.

agreement with the DNS data for $y^{\times} < 2$ approximately. The outer scaling, however, exhibits a rather poor agreement with the computed DNS profiles. The outer scaling velocity profile was found to the be very sensitive to the empirically calibrated coefficients. This is a very undesirable feature when aiming at universal scaling laws that could be used as wall functions for CFD. Such observation justifies the direction taken in recent years by the turbulence modelling community focusing now on wall integrated approaches instead of wall functions. Since no obvious advantage was found when plotting the results using scaling parameters specific to buoyancy driven flows [51,52,54], classic viscous wall units denoted by the superscript + are used in the remainder of the paper. A summary of the normalisation factors applied to convert various quantities based on the normalisation given by Eq. 4 into wall units is given in Table 3.

Second order statistical moments are given at different cavity heights in Figs. 10, 12 and 14. The $\overline{u'u'}$ profile tends to exhibit some degree of self similarity in the upper part of the boundary layer where the turbulence is most developed. At the highest Rayleigh number, an intermediate region with an almost constant value of $\overline{u'u'}$ does appear. The values of $\overline{v'v'}$ and $\overline{w'w'}$ for the case at $Ra = 10^8$ are extremely small when compared to the streamwise component $\overline{u'u'}$, which confirms that the fluctuations are mainly caused by the streamwise motion of the buoyant plumes rising along the vertical wall. As regards the $\overline{w'w'}$ component, which was rarely shown in previous cavity publications, the maximum is located in the outer layer, at the edge of the quiescent stratification. The shear stress component $\overline{u'v'}$ exhibits, at the three highest Rayleigh numbers, a negative region in the vicinity of the wall before becoming positive. This feature in the near wall region was also observed by Barhaghi and Davidson [36] in the tall 5:1 cavity and by Versteegh and Nieuwstadt [33] in the infinite vertical channel. As it will be seen in the next section, the explanation for such phenomenon lies in the sign of the total production of shear stress $\overline{u'v'}$ near the wall. As regards the turbulent heat fluxes, a mild negative near wall region appears at the highest Rayleigh number for the $\overline{u'\theta'}$ component. Similar observation was made by Barhaghi and Davidson [36] in the transitional region of their boundary layer but not in the developed part as observed here.

A very important aspect of buoyant boundary layers, which has significant consequences on the variation of the production terms in the budgets, is the relative position of Reynolds stresses and turbulent heat fluxes extrema within the boundary layer. In a forced convection boundary layer all the Reynolds stresses and turbulent heat fluxes maxima are located within the buffer layer. In the case of a differentially heated infinite vertical channel, all the Reynolds stresses are maximum in the middle of the channel. In the present case the situation is rather different as illustrated in Figs. 11 and 13. At the lowest Rayleigh number all the maxima are located in the outer layer (beyond the velocity maximum) with the turbulent heat fluxes and temperature variance extrema remaining close the velocity maximum. The $\overline{v'v'}$ and $\overline{u'v'}$ extrema are the furthest from the wall and close to the outer edge of the boundary layer. These observations are in agreement with Barhaghi and Davidson [36]. When the Rayleigh number is increased, the $\overline{v'v'}$ and $\overline{u'v'}$ maxima tend to follow each other and to move further away from the velocity maximum whilst the components $\overline{u'\theta'}$, $\overline{v'\theta'}$ and $\overline{\theta'\theta'}$ tend to remain near it. The maximum of $\overline{u'u'}$ is located in a more intermediate position approximately between the velocity maximum and the position of the $\overline{v'v'}$ and $\overline{u'v'}$ maxima at the edge of the boundary layer.

3.4. Turbulence budgets

First and second order moments are very important quantities to provide engineering predictions but they are not sufficient on their own to help the development of new turbulence models. The term by term analysis of the transport equations usually modelled and solved within the Reynolds averaged (RANS) framework is very important. Analysis of the turbulence budget in forced convection channel flows has been the backbone of turbulence modelling in the last decades. However, there is little attention given in the literature to such data for buoyancy driven flows. Boudjemadi et al. [55], Versteegh and Nieuwstadt [33] and more recently Kis and Herwig [35] computed the full turbulence budgets at moderate Rayleigh number in a vertical differentially heated channel. To the authors' knowledge only the LES calculation of Barhaghi and Davidson [36] for a 5:1 vertical differentially heated cavity presents partial, qualitative budgets for natural convection in a differentially heated enclosure. In the following section each term in the *exact* transport equation for the Reynolds stresses, turbulent kinetic energy, turbulent heat flux and temperature variance are presented. As the mean flow varies spatially in two spatial dimensions, the budgets will be analysed only at $x = 0.8$ in the vicinity of the hot wall where the vertical buoyant boundary layer is most developed. In order

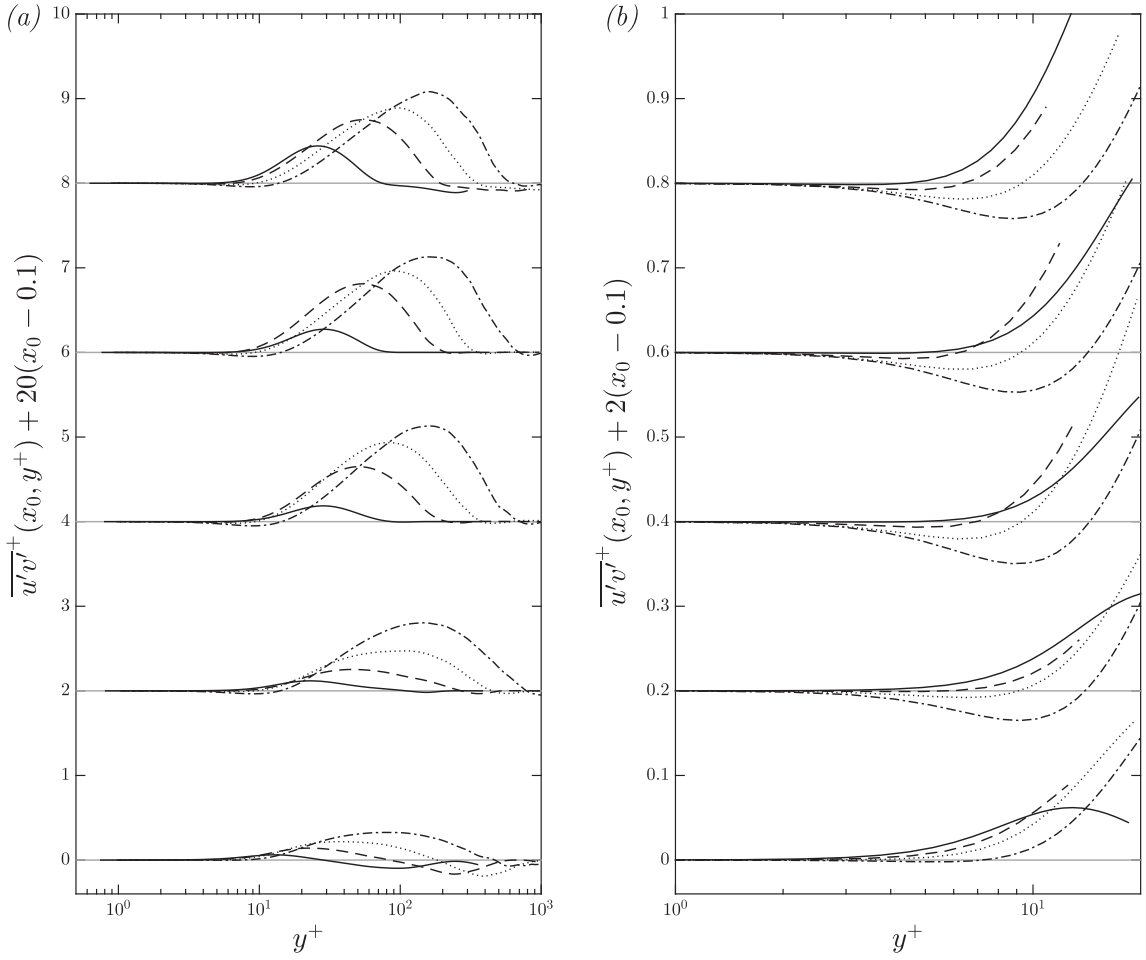

Fig. 14. Comparison of Reynolds shear stress $\overline{u'v'}$at different cavity heights ($x_0 = 0.1 - 0.3 - 0.5 - 0.7 - 0.9$) (——— $Ra = 10^8$ — — — $Ra = 1.58 \times 10^9$ - - - - - $Ra = 10^{10}$ — · — $Ra = 10^{11}$): (a) Full profile in the vicinity of the hot wall (b) zoom on the near wall profile exhibiting negative shear stress regions.

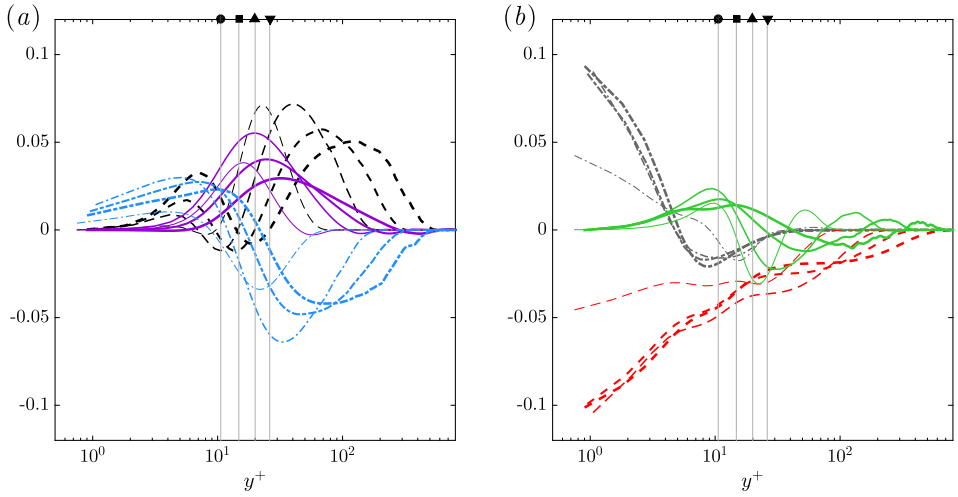

Fig. 15. Comparison of the budget of $\overline{u'u'}^+$ at $x = 0.8$: (a) P_{11}^+ G_{11}^+ Π_{11}^+ (b) $-\varepsilon_{11}^+$ $D_{11}^{t^+}$ $D_{11}^{\nu^+}$. The different Rayleigh numbers are indicated by different line thickness (——— $Ra = 10^8$ ——— $Ra = 1.58 \times 10^9$ ——— $Ra = 10^{10}$ ——— $Ra = 10^{11}$) Vertical lines indicate the position of the velocity maximum at given x-position: •$Ra = 10^8$ ■ $Ra = 1.58 \times 10^9$ ▲ $Ra = 10^{10}$ ▼ $Ra = 10^{11}$).

to illustrate the spatial evolution of the flow along the hot wall boundary layer, the budget of turbulent kinetic energy will be presented at three cavity heights $x = 0.2, x = 0.5$ and $x = 0.8$. The associated database contains the complete statistical data at multiple positions in the cavity.

In what follows, the term *inner layer* will be used to denote the region of the buoyant boundary layer between the wall and the velocity maximum and the term *outer layer* will be used to denote the region extending from the velocity maximum to the quiescent cavity core.

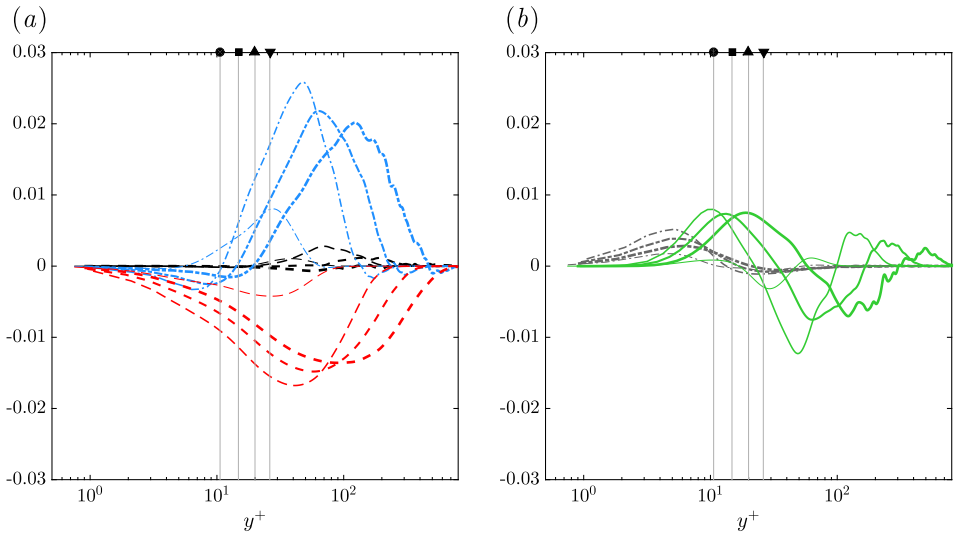

Fig. 16. Comparison of the budget of $\overline{v'v'}^+$ at $x = 0.8$: (a) P_{22}^+ Π_{22}^+ $-\varepsilon_{22}^+$ (b) $D_{22}^{t^+}$ $D_{22}^{v^+}$. The different Rayleigh numbers are indicated by different line thickness ($Ra = 10^8$ $Ra = 1.58 \times 10^9$ $Ra = 10^{10}$ $Ra = 10^{11}$) Vertical lines indicate the position of the velocity maximum at given x-position: •$Ra = 10^8$ ■ $Ra = 1.58 \times 10^9$ ▲ $Ra = 10^{10}$ ▼$Ra = 10^{11}$).

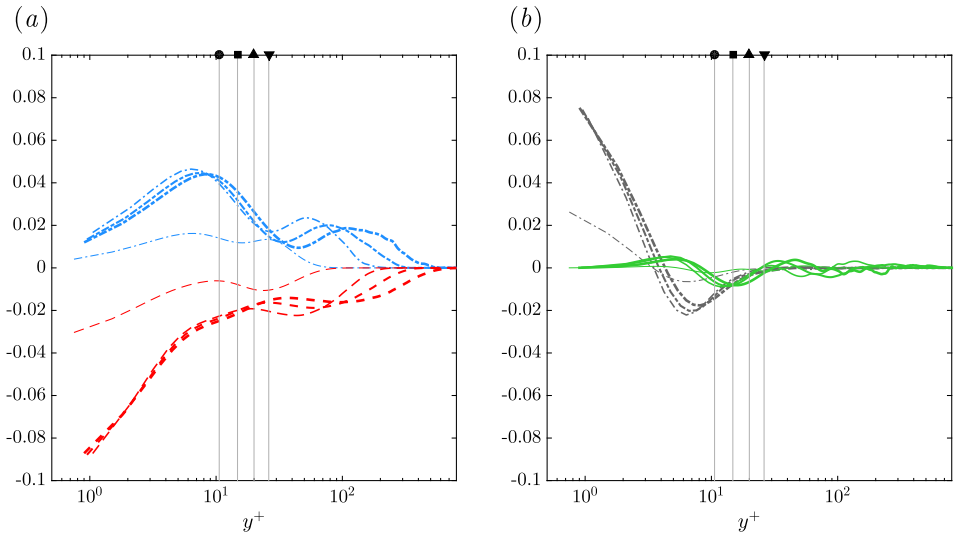

Fig. 17. Comparison of the budget of $\overline{w'w'}^+$ at $x = 0.8$: (a) Π_{33}^+ $-\varepsilon_{33}^+$ (b) $D_{33}^{t^+}$ $D_{33}^{v^+}$. The different Rayleigh numbers are indicated by different line thickness ($Ra = 10^8$ $Ra = 1.58 \times 10^9$ $Ra = 10^{10}$ $Ra = 10^{11}$) Vertical lines indicate the position of the velocity maximum at given x-position: •$Ra = 10^8$ ■ $Ra = 1.58 \times 10^9$ ▲ $Ra = 10^{10}$ ▼ $Ra = 10^{11}$).

3.4.1. Reynolds stress budgets

The *exact* Reynolds stress transport equation using the normalised formulation of the Navier–Stokes equations introduced earlier is given by:

$$\frac{\partial \overline{u_i' u_j'}}{\partial t} + \underbrace{U_k \frac{\overline{u_i' u_j'}}{\partial x_k}}_{C_{ij}} = \underbrace{-\left(\overline{u_i' u_k'} \frac{\partial U_j}{\partial x_k} + \overline{u_j' u_k'} \frac{\partial U_i}{\partial x_k}\right)}_{P_{ij}} \underbrace{-Pr\left(\overline{u_j' \theta'} g_i + \overline{u_i' \theta'} g_j\right)}_{G_{ij}} \underbrace{-\left(\overline{u_i' \frac{\partial p'}{\partial x_j}} + \overline{u_j' \frac{\partial p'}{\partial x_i}}\right)}_{\Pi_{ij}} \underbrace{-\frac{2Pr}{Ra^{1/2}} \overline{\frac{\partial u_i'}{\partial x_k} \frac{\partial u_j'}{\partial x_k}}}_{\varepsilon_{ij}} + \underbrace{\frac{Pr}{Ra^{1/2}} \frac{\partial^2 \overline{u_i' u_j'}}{\partial x_k \partial x_k}}_{D_{ij}^v} \underbrace{-\frac{\partial \overline{u_i' u_j' u_k'}}{\partial x_k}}_{D_{ij}^t} \quad (17)$$

Each of the terms in the above equation can be determined from the results of the DNS and all the budgets are plotted using the classic viscous wall units normalisation as presented in Table 3. The convective terms C_{ij} are not represented as they are very small and tend to reduce the clarity of the graphs presented below. However, all the terms are included in the database for completeness.

The budget of the component $\overline{u'u'}$ is given in Fig. 15. In the vicinity of the wall ($y^+ < 3$), the turbulent dissipation ε_{11} is balanced by the viscous diffusion D_{11}^v and pressure redistribution term Π_{11}. At the wall the pressure redistribution term vanishes and therefore ε_{11} and D_{11}^v are exactly in balance, which is expected when considering the Taylor series expansion of the budget terms near the wall. The production by shear has a very interesting profile with two peaks and a negative region in between. It can be approximated by the following dominant term:

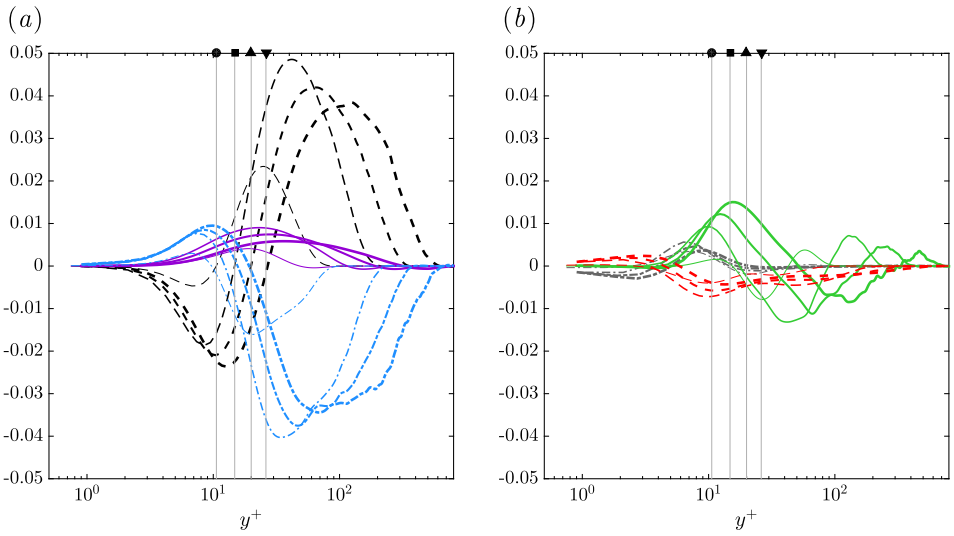

Fig. 18. Comparison of the budget of $\overline{u'v'}^+$ at $x = 0.8$: (a) P_{12}^+ G_{12}^+ Π_{12}^+ (b) $-\varepsilon_{12}^+$ $D_{12}^{t^+}$ $D_{12}^{\nu^+}$. The different Rayleigh numbers are indicated by different line thickness ($Ra = 10^8$ $Ra = 1.58 \times 10^9$ $Ra = 10^{10}$ $Ra = 10^{11}$) Vertical lines indicate the position of the velocity maximum at given x-position: •$Ra = 10^8$ ■ $Ra = 1.58 \times 10^9$ ▲ $Ra = 10^{10}$ ▼ $Ra = 10^{11}$).

$$P_{11} \approx -2\overline{u'v'}\frac{\partial U}{\partial y} \tag{18}$$

The first peak in the inner layer is explained by the existence of a region of negative shear stress $\overline{u'v'}$ near the wall, for sufficiently high Rayleigh numbers. For all Rayleigh numbers the change of sign of the shear stress $\overline{u'v'}$ occurs before the velocity maximum, thus yielding a negative P_{11} region since both $\overline{u'v'}$ and $\partial U/\partial y$ are positive. As the Rayleigh number is increased, the distance from the vertical wall at which the turbulent shear stress becomes positive tends to increase. At the same time, the point where the vertical velocity reaches its maximum gets closer to the walls. The combination of both of these effects yields a narrowing of the region where both $\overline{u'v'}$ and $\partial U/\partial y$ are positive, which explains why the region where P_{11} is negative tend to disappear as the Rayleigh number increases.

The $\overline{v'v'}$ component of the Reynolds stress tensor is a very small contributor to the total turbulent kinetic energy, which is dominated by the $\overline{u'u'}$ term discussed above, but remains important. Indeed, this component appears in the production term of the shear stress $\overline{u'v'}$. The budget of $\overline{v'v'}$, showed in Fig. 16, is the most difficult to compute accurately and the slowest to converge statistically. In the near wall region, all the terms tend to zero asymptotically and very close to the wall ($y^+ < 5$) the turbulent dissipation ε_{22} is balanced by the viscous diffusion term D_{22}^{ν}. The shear production P_{22} is very small since the mean velocity V is very close to zero in most of the boundary layer. In the outer part of the boundary layer, the two dominant terms are the pressure redistribution term Π_{22} and the dissipation term ε_{22}. Π_{22} acts as a source term redistributing energy from the $\overline{u'u'}$ component where turbulence is produced by shear and buoyancy. The turbulent diffusion term D_{22}^{t} is significant and reaches a negative minimum when the pressure redistribution term is highest. This term thus acts as a draining term helping the transfer of energy from the highly turbulent central region of the boundary layer to both the inner layer and outer edge of the boundary layer.

The budget of $\overline{w'w'}$ is given in Fig. 17. Because of the spanwise homogeneity of the present flow, the production terms P_{33} and G_{33} in the budget of $\overline{w'w'}$ are exactly zero. At the wall the viscous diffusion D_{33}^{ν} exactly balances the turbulence dissipation ε_{33}. The main source term is the pressure redistribution term Π_{33}. Away from the wall, this term is in balance with the dissipation rate ε_{33} and all other terms in the budget are zero or negligible.

The budget of $\overline{u'v'}$ is the only other component where the terms of production by shear and buoyancy are not zero or negligible. The production by shear can be approximated by the following:

$$P_{12} \approx -\overline{v'v'}\frac{\partial U}{\partial y} \tag{19}$$

The Reynolds stress $\overline{v'v'}$ is positive over the entire buoyant boundary layer by definition. In the inner part of the boundary layer the gradient of velocity $\partial U/\partial y$ is positive thus yielding the negative production P_{12} as observed in Fig. 18. Beyond the position of the velocity maximum, the gradient $\partial U/\partial y$ becomes negative yielding a positive shear production term. The buoyancy production is proportional to the turbulent heat flux component $\overline{v'\theta'}$, which has a magnitude approximately three times smaller than the other turbulent heat flux component $\overline{u'\theta'}$. The direct consequence is that the buoyancy production term G_{12} has a fairly small magnitude when compared to the shear production P_{12} term. This was not the case for the $\overline{u'u'}$ budget. In addition to this, the total production $(P_{12} + G_{12})$ is negative in the inner layer, which is consistent with the negative shear stress observed earlier as illustrated in Fig. 14. When the Rayleigh number is increased, the negative shear production region in the inner layer becomes more pronounced whereas the positive shear production region in the outer layer tends to decrease. In the outer layer the pressure term acts as a sink term compensating almost the entire shear production. To a lesser extent, the turbulent diffusion D_{12}^{t} also acts as a draining term when the shear production is maximum and transfers energy to the outer edge of the boundary layer and around the location of the maximum velocity.

3.4.2. Turbulence kinetic energy budget

Classic two-equation turbulence models include a transport equation for the turbulent kinetic energy. The exact form of the equation given in Eq. (20) is obtained by taking one half of the sum of the exact transport equations for the diagonal terms of the Reynolds stress tensor:

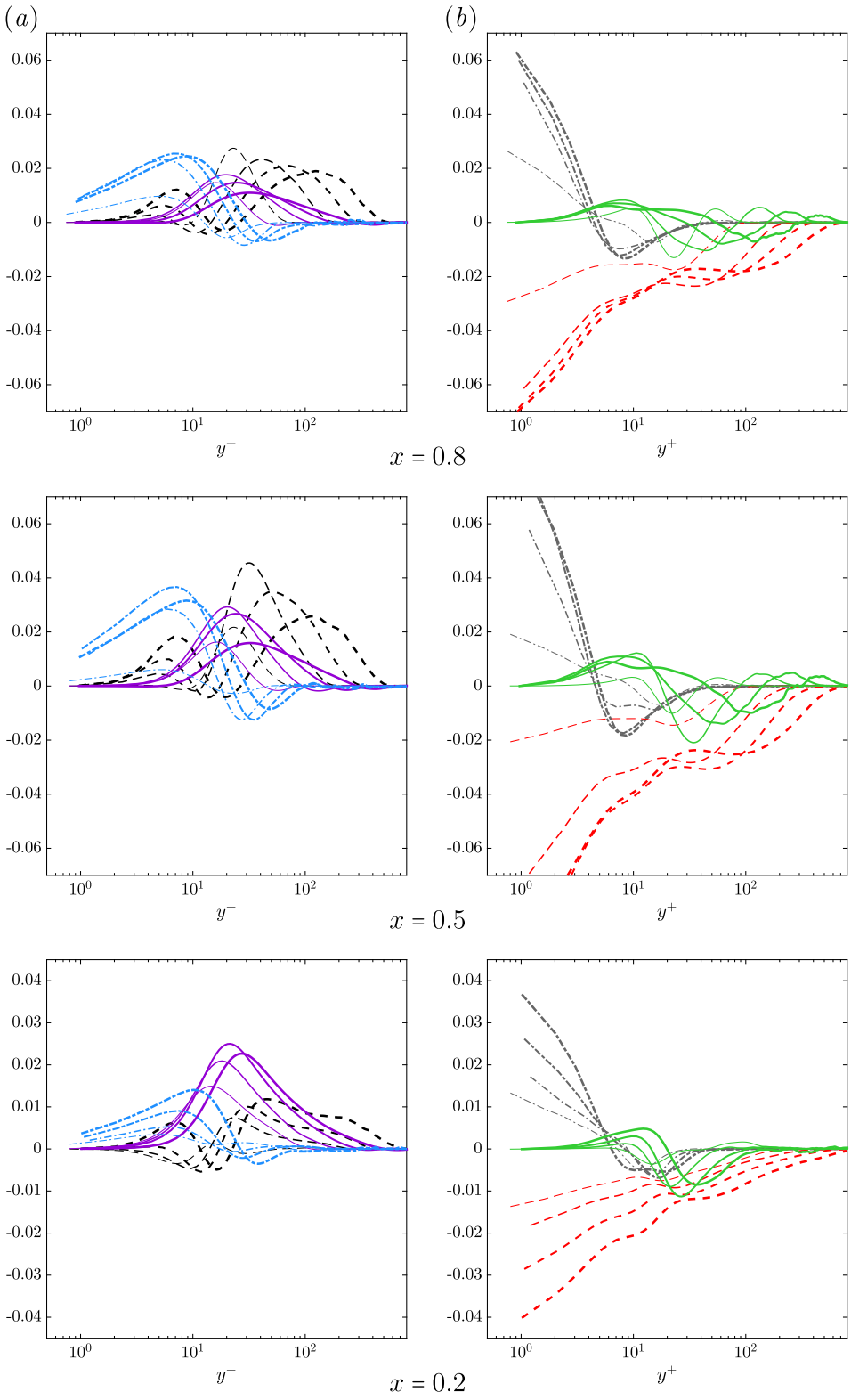

Fig. 19. Comparison of the budget of turbulent kinetic energy k^+ at $x = 0.2, 0.5, 0.8$ in the vicinity of the hot wall : (a) P_k^+ G_k^+ $D_k^{p^+}$ (b) $-\varepsilon^+$ $D_k^{\nu^+}$ $D_k^{\nu^+}$. The different Rayleigh numbers are indicated by different line thickness ($Ra = 10^8$ $Ra = 1.58 \times 10^9$ $Ra = 10^{10}$ $Ra = 10^{11}$).

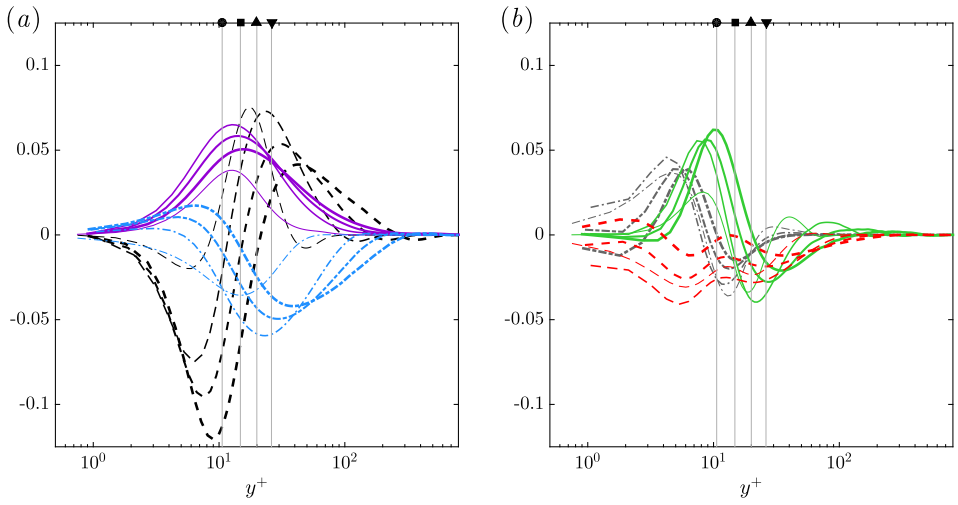

Fig. 20. Comparison of the budget of $\overline{u'\theta'}^+$ at $x = 0.8$: (a) $P^+_{\theta 1}$ $G^+_{\theta 1}$ $\Pi^+_{\theta 1}$ (b) $-\varepsilon^+_{\theta 1}$ $D^{t^+}_{\theta 1}$ $D^{\nu^+}_{\theta 1} + D^{\alpha^+}_{\theta 1}$. The different Rayleigh numbers are indicated by different line thickness ($Ra = 10^8$ $Ra = 1.58 \times 10^9$ $Ra = 10^{10}$ $Ra = 10^{11}$).

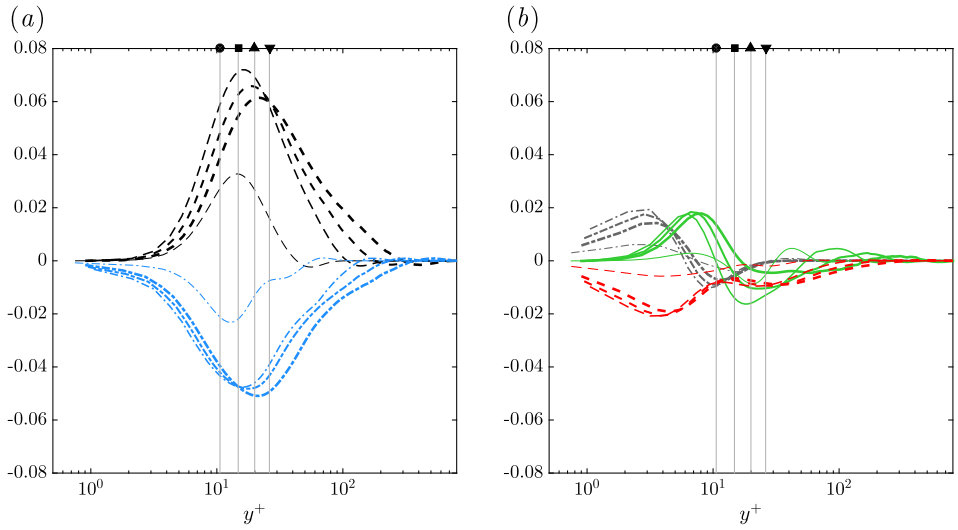

Fig. 21. Comparison of the budget of $\overline{v'\theta'}^+$ at $x = 0.8$: (a) $P^+_{\theta 2}$ $\Pi^+_{\theta 2}$ (b) $-\varepsilon^+_{\theta 2}$ $D^{t^+}_{\theta 2}$ $D^{\nu^+}_{\theta 2} + D^{\alpha^+}_{\theta 2}$. The different Rayleigh numbers are indicated by different line thickness ($Ra = 10^8$ $Ra = 1.58 \times 10^9$ $Ra = 10^{10}$ $Ra = 10^{11}$).

$$\frac{\partial k}{\partial t} + \underbrace{U_j \frac{\partial k}{\partial x_j}}_{C_k} = \underbrace{-\overline{u_i' u_j'} \frac{\partial U_i}{\partial x_j}}_{P_k} \underbrace{-Pr\, \overline{u_i' \theta'} g_i}_{G_k} \underbrace{-\frac{\partial \overline{u_i' p'}}{\partial x_i}}_{D_k^p} \underbrace{-\frac{Pr}{Ra^{1/2}} \frac{\overline{\partial u_i'}}{\partial x_j} \frac{\partial u_i'}{\partial x_j}}_{\varepsilon} + \underbrace{\frac{Pr}{Ra^{1/2}} \frac{\partial^2 k}{\partial x_j \partial x_j}}_{D_k^\nu} \underbrace{-\frac{1}{2} \frac{\partial \overline{u_i' u_i' u_j'}}{\partial x_j}}_{D_{ij}^t} \tag{20}$$

The spatial evolution of the turbulent kinetic energy budget along the hot wall buoyant boundary layer is illustrated in Fig. 19. As mentioned earlier, along the hot wall, the largest contributor to the kinetic energy budget is the $\overline{u'u'}$ component. This explains the large similarity between the budget of kinetic energy and the budget of $\overline{u'u'}$ at the same location in Fig. 15.

Budget Eq. (17) was written without the historical split of velocity-pressure gradient Π_{ij} as the sum of pressure-diffusion and pressure-strain. As the latter is traceless, only pressure diffusion remains in the turbulent kinetic energy budget. The pressure diffusion term D_k^p arises from the wall normal pressure diffusion D_{22}^p. The observed contribution of the pressure diffusion term D_k^p near the wall is much larger than in a fully developed channel flow where this term is almost negligible when compared to other terms.

As regards the spatial development of the turbulent kinetic energy budget term, the most important aspect is the magnitude of the buoyancy production in the lower part of the cavity ($x = 0.2$). This term is actually the dominant production mechanism in the boundary layer. From a turbulence modelling perspective, this means that underestimation of $\overline{u'\theta'}$ will lead to a serious under prediction in the turbulent kinetic energy level and most probably a delay in the location of turbulence enhancement observed in Fig. 5b and in the local extrema in Nusselt number illustrated in Fig. 4.

3.4.3. Turbulent heat flux budgets

The transport equation for turbulent heat flux $\overline{u'\theta'}$ is given in Eq. (21) and its budget presented in Fig. 20. Barhaghi and Davidson

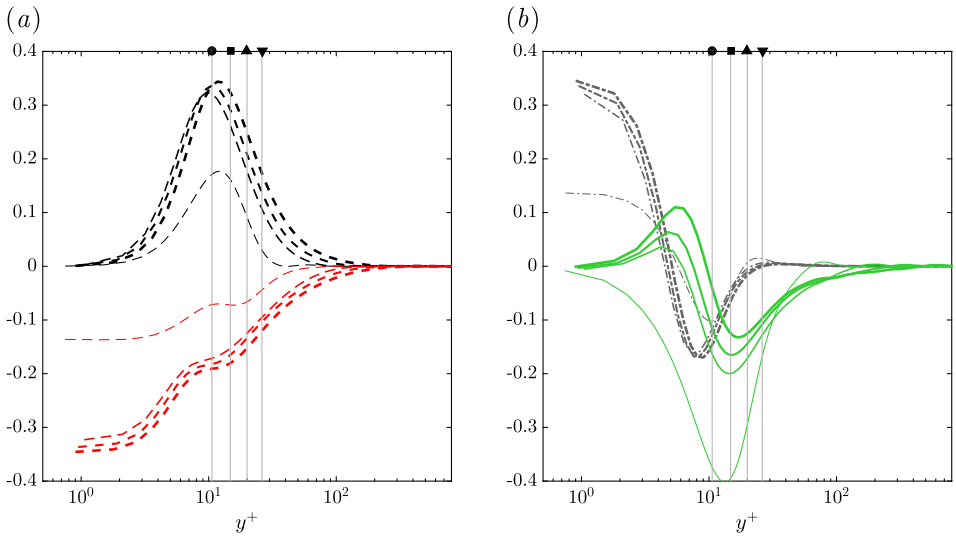

Fig. 22. Comparison of the budget of $\overline{\theta'\theta'}^+$ at $x = 0.8$: (a) $P^+_{\theta\theta}$ $-\varepsilon^+_{\theta\theta}$(b) $D^{t^+}_{\theta\theta}$ $D^{\alpha^+}_{\theta\theta}$. The different Rayleigh numbers are indicated by different line thickness ($Ra = 10^8$ $Ra = 1.58 \times 10^9$ $Ra = 10^{10}$ $Ra = 10^{11}$).

[36] did not provide the budget for this component arguing it is unimportant, because in the mean temperature equation solved in a RANS framework, this term vanishes in the divergence of the turbulent heat fluxes. However, as discussed earlier, this component was shown to be very important for the predictions of the buoyancy production term both in the $\overline{u'u'}$ budget and more importantly in the turbulent kinetic energy budget. The term is therefore extremely important even within the common framework of two-equations based eddy-viscosity models.

$$\underbrace{\frac{\partial \overline{u_i'\theta'}}{\partial t} + \underbrace{U_j \frac{\overline{u_i'\theta'}}{\partial x_j}}_{C_{\theta i}}}_{} = \underbrace{-\left(\overline{u_i'u_j'}\frac{\partial \Theta}{\partial x_j} + \overline{u_j'\theta'}\frac{\partial U_i}{\partial x_j}\right)}_{P_{\theta i}} \underbrace{- Pr g_i \overline{\theta'\theta'}}_{G_{\theta i}} \underbrace{- \left(\overline{\theta'\frac{\partial p'}{\partial x_i}}\right)}_{\Pi_{\theta i}} \underbrace{- \left(\frac{Pr}{Ra^{1/2}} + \frac{1}{Ra^{1/2}}\right)\overline{\frac{\partial \theta'}{\partial x_j}\frac{\partial u_i'}{\partial x_j}}}_{-\varepsilon_{\theta i}}$$
$$\underbrace{+ \frac{1}{Ra^{1/2}}\left(\overline{\frac{\partial u_i'}{\partial x_j}\frac{\partial \theta'}{\partial x_j}} + \overline{u_i'\frac{\partial^2 \theta'}{\partial x_j \partial x_j}}\right)}_{D^{\alpha}_{\theta i}} \underbrace{+ \frac{Pr}{Ra^{1/2}}\left(\overline{\frac{\partial \theta'}{\partial x_j}\frac{\partial u_i'}{\partial x_j}} + \overline{\theta'\frac{\partial^2 u_i'}{\partial x_j \partial x_j}}\right)}_{D^{\nu}_{\theta i}} \underbrace{- \overline{\frac{\partial \theta' u_i' u_k'}{\partial x_j}}}_{D^{t}_{\theta i}} \tag{21}$$

The shear production term exhibits a negative minimum in the inner layer and a positive maximum in the outer layer. This production term can be approximated as follows:

$$P_{\theta 1} \approx -\overline{u'v'}\frac{\partial \Theta}{\partial y} - \overline{v'\theta'}\frac{\partial U}{\partial y} \tag{22}$$

Both terms in Eq. (22) are important. The large negative values in the inner region mostly arises from the second term in Eq. (22) because $\overline{v'\theta'}$ is positive across the entire boundary layer and $\partial U/\partial y$ is positive in the inner layer. Since $\partial\Theta/\partial y$ is negative up to the edge of the outer layer, the first term can also be negative in the vicinity of the wall in the case where $\overline{u'v'}$ is negative. This occurs only at the highest Rayleigh numbers as seen in Fig. 14. This explains the amplification of the negative production region as the Rayleigh number is increased. The second aspect that tends to contribute to this phenomena is the position of the maximum of $\overline{v'\theta'}$ illustrated in Figs. 11 and 13. For all Rayleigh numbers the maximum of $\overline{v'\theta'}$ is in the outer layer but as the Rayleigh number is increased, the gap between the maximum velocity and the maximum of $\overline{v'\theta'}$ tends to reduce. This yields higher value of $\overline{v'\theta'}$ in the region where $\partial U/\partial y$ is positive, therefore enhancing the negative contribution of the second term in Eq. (22).

Table 4
Summary of the simulation parameters used for the simulation of the Trias cavity.

Ra	2×10^9
Pr	0.71
$(L_x/H, L_y/H, L_z/H)$	$(1.0, 0.25, 0.25)$
(N_x, N_y, N_z)	$(1025, 513, 128)$
Δt	6×10^{-4}
β_s	0.05
Δt_{dev}	250
Δt_{avg}	550

In comparison, the budget of $\overline{v'\theta'}$ is much simpler as shown in Fig. 21. The two dominant terms in balance are the production $P_{\theta 2}$ and the pressure term $\Pi_{\theta 2}$. The production term $P_{\theta 2}$ can be approximated as follows:

$$P_{\theta 2} \approx -\overline{v'v'}\frac{\partial \Theta}{\partial y} \tag{23}$$

The variation of temperature gradient are significant only in the outer region of the boundary layer, which explains why the $P_{\theta 2}$ profile resembles the $\overline{v'v'}$ profile for approximately $y^+ < 10$. The other terms of the budget are mostly negligible for $y^+ > 10$. Very close to the wall, the turbulent dissipation $\varepsilon_{\theta 2}$ is in balance with the viscous diffusion term $D^{\nu}_{\theta 2}$. In the outer layer, as the Rayleigh number increases, the magnitude of the turbulent diffusion term $D^{t}_{\theta 2}$ tends to decrease.

3.4.4. Temperature variance budget

The normalised transport equation for temperature variance $\overline{\theta'\theta'}$ is given in Eq. (24). The associated budget is shown in Fig. 22.

$$\underbrace{\frac{\partial \overline{\theta'\theta'}}{\partial t} + \underbrace{U_k \frac{\overline{\theta'\theta'}}{\partial x_k}}_{C_{\theta\theta}}}_{} = \underbrace{-2\left(\overline{\theta' u_k'}\frac{\partial \Theta}{\partial x_k}\right)}_{P_{\theta\theta}} \underbrace{- \frac{2}{Ra^{1/2}}\overline{\frac{\partial \theta'}{\partial x_k}\frac{\partial \theta'}{\partial x_k}}}_{-\varepsilon_{\theta\theta}} \underbrace{+ \frac{1}{Ra^{1/2}}\frac{\partial^2 \overline{\theta'\theta'}}{\partial x_k \partial x_k}}_{D^{\alpha}_{\theta\theta}} \underbrace{+ \frac{\partial \overline{\theta'\theta' u_k}}{\partial x_k}}_{D^{t}_{\theta\theta}} \tag{24}$$

Apart from the lowest Rayleigh number, the temperature variance presents the highest level of self-similarity among all the budgets based on the present wall units inner scaling. This is in

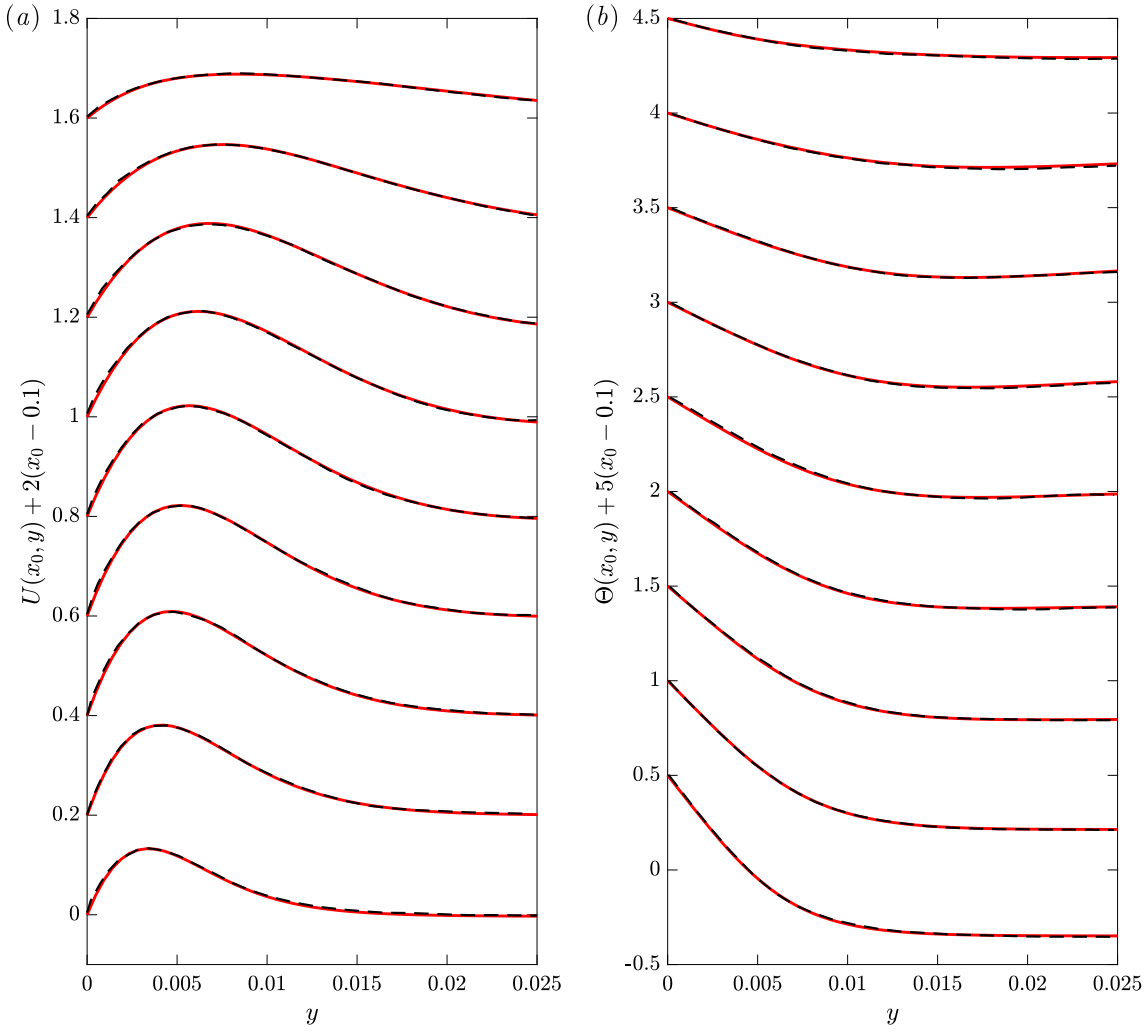

Fig. 23. Comparison of the first order moments against the DNS data of Trias [19] at different cavity heights ($x_0 = 0.1 - 0.2 - 0.3 - 0.4 - 0.5 - 0.6 - 0.7 - 0.8 - 0.9$): (a) Mean vertical velocity U (b) Mean temperature Θ (– – – Data of Trias ——— Present simulation).

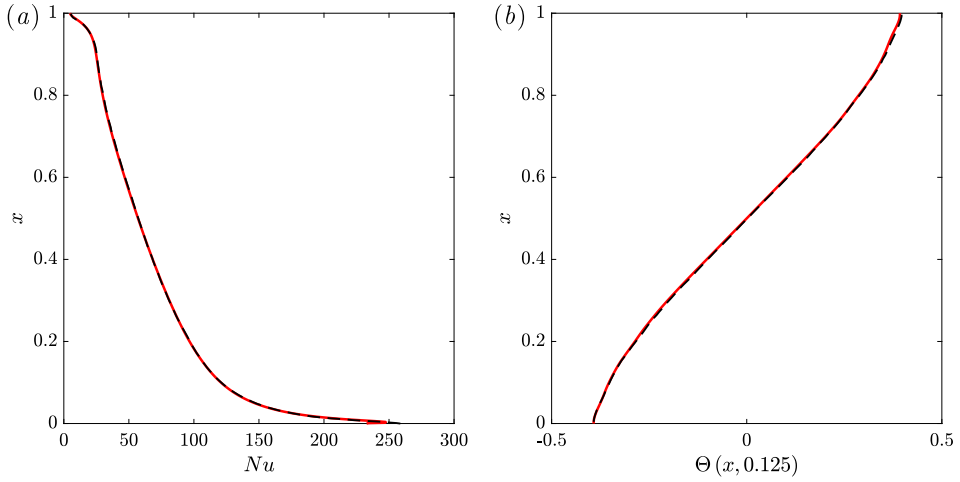

Fig. 24. Comparison of the Nusselt number and temperature stratification against the DNS data of Trias [19]: (a) Mean Nusselt number $Nu(x, 0)$ (b) Mean temperature stratification $\Theta(x, 0.125)$ (– – – Data of Trias ——— Present simulation).

Table 5
Summary of the simulations used to assess the grid-dependence of the results. Same notation as in Fig. 1 and Table 1 are used.

Simulation	L_z/H	$N_x \times N_y \times N_z$	β_s	Δt	Δt_{dev}	Δt_{avg}
Mesh 1	0.8	$513 \times 513 \times 128$	0.12	1.0×10^{-3}	100	125
Mesh 2	0.4	$1025 \times 1025 \times 64$	0.12	2.5×10^{-4}	20	100
Mesh 3	0.4	$1025 \times 513 \times 128$	0.1	7×10^{-4}	20	160

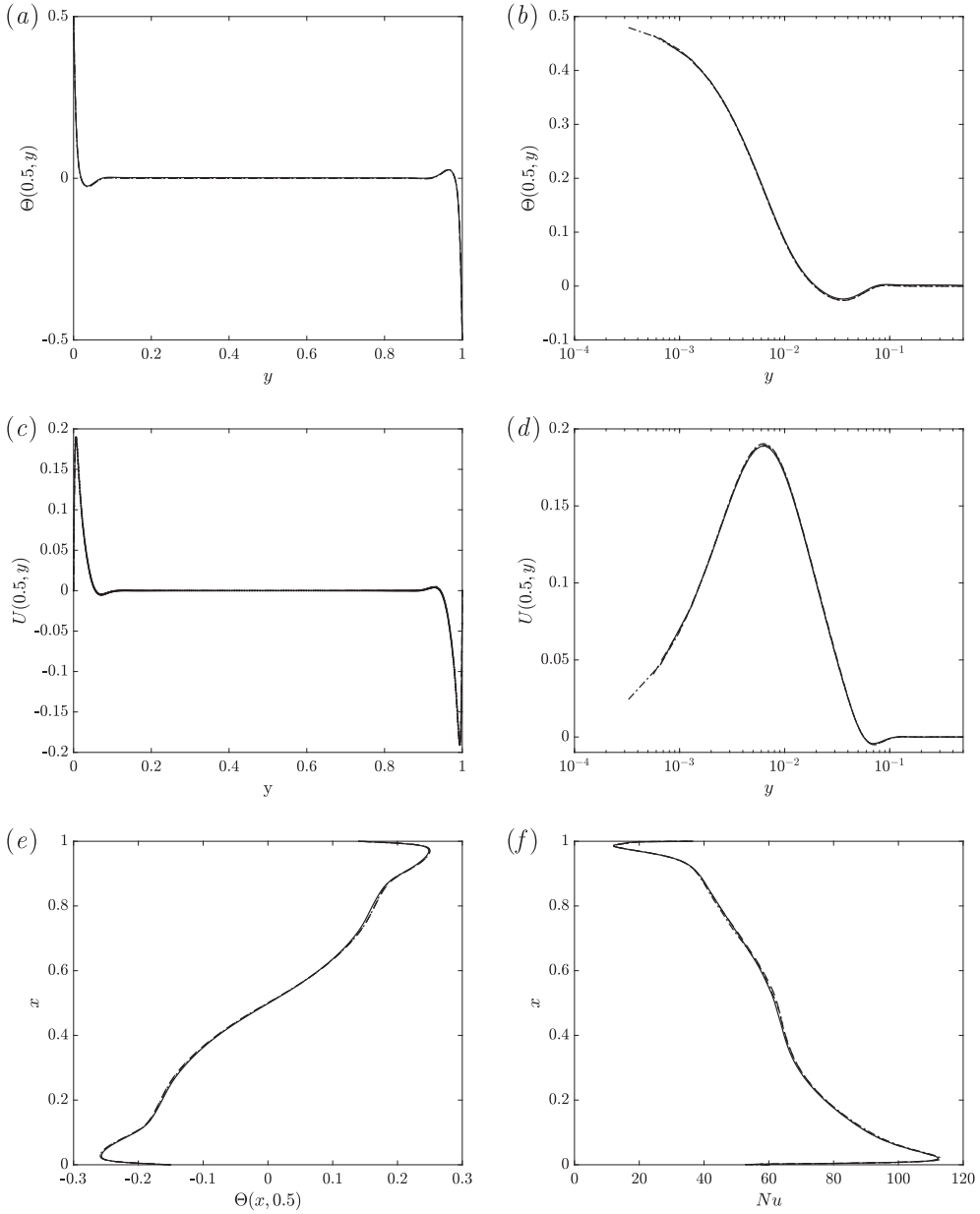

Fig. 25. First order moments comparison between meshes (——— Mesh 1 — · — Mesh 2 — — — Mesh 3): (a) and (b) Mean temperature at cavity mid-height; (c) and (d) Mean vertical velocity at cavity mid-height; (e) Mean temperature profile at cavity mid-width; (f) Nusselt number on the hot wall.

agreement with the observations made earlier about the mean temperature and temperature variance profiles. The production term $P_{\theta\theta}$ can be approximated:

$$P_{\theta\theta} \approx -\overline{v'\theta'}\frac{\partial \Theta}{\partial y} \tag{25}$$

The peak of production is in the outer layer for all Rayleigh numbers except 10^8, which is in agreement with the observations made in Figs. 11 and 13 regarding the position of the maximum of temperature variance. Near the wall, as expected from the Taylor expansion of the budget terms, the turbulent dissipation $\varepsilon_{\theta\theta}$ and the viscous diffusion $D^v_{\theta\theta}$ are dominant and exactly in balance at the wall. The turbulent diffusion term $D^t_{\theta\theta}$ is non negligible, even at the highest Rayleigh number and acts as a sink term around the location of the production extrema. It redistributes energy to the inner layer, which is represented by a maximum around $y^+ \approx 5$.

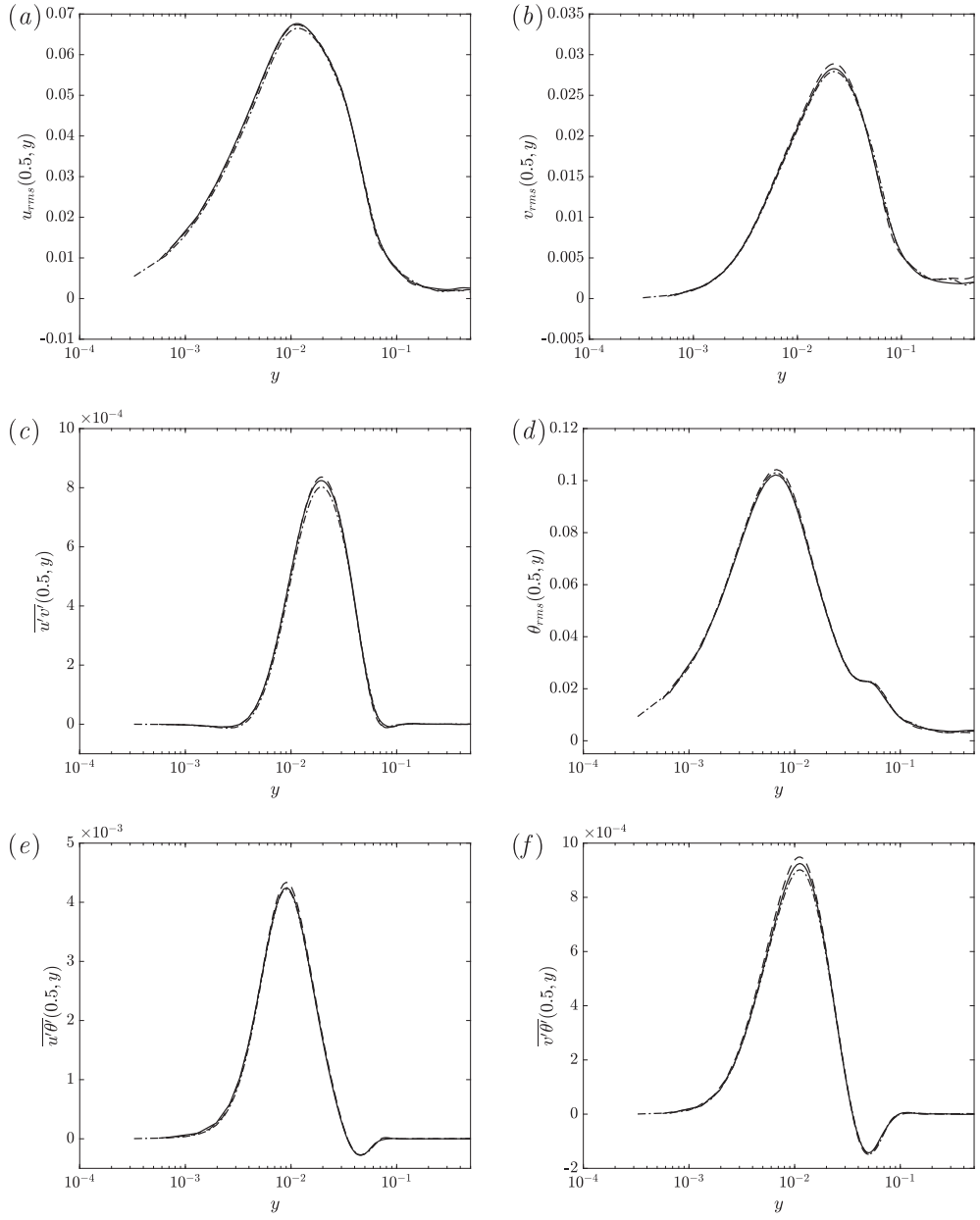

Fig. 26. Second order moments comparison at cavity mid-height in the vicinity of the hot wall (——— Mesh 1 — · — Mesh 2 — — — Mesh 3): (a) u_{rms} (b) v_{rms} (c) $\overline{u'v'}$ (d) θ_{rms} (e) $\overline{u'\theta'}$ (f) $\overline{v'\theta'}$.

4. Conclusion

In the present paper, a set of highly resolved Direct Numerical Simulations was carried out in a differentially heated cavity under the Boussinesq approximation for Prandtl number $Pr = 0.71$ and Rayleigh numbers ranging between 10^8 and 10^{11}. This includes the highest Rayleigh number ever reached numerically in a square cavity configuration.

High Rayleigh number effects were investigated in the more ideal configuration where a linear temperature variation is prescribed on the horizontal walls. The computations include first and second order statistical moments as well as the full budgets of all second order moments. These budgets revealed the importance of the buoyancy production terms over the entire range of Rayleigh numbers covered in the present paper. This highlights the importance of the modelling of the turbulent heat flux component perpendicular to the temperature gradient, which is known to be the most difficult to represent accurately. Another interesting observation arose from the simulation at the highest Rayleigh number. A negative region of $\overline{u'\theta'}$ appeared in the vicinity of the vertical wall for $Ra = 10^{11}$. Such negative values of streamwise heat flux were observed in 5:1 cavities by both Barhaghi and Davidson [36] and Trias et al. [20,21], but only in the transitional range of their boundary layers. In the present case, this is observed in the part of the boundary layer where turbulence is most developed.

The motivation for the present paper was to contribute to the understanding of the flow physics in square differentially heated cavity from a turbulence modelling perspective, knowing that this configuration has been, over the years, one of the most challenging

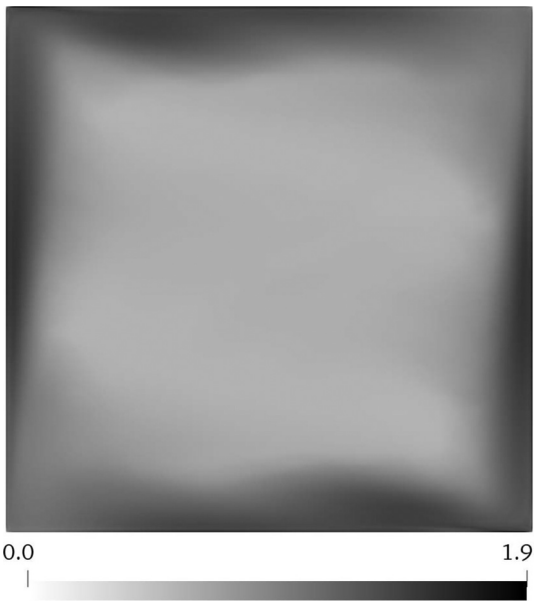

Fig. 27. Computed grid to Kolmogorov length scale ratio $(\Delta x \Delta y \Delta z)^{1/3}/\eta$ obtained for the simulation on mesh 3.

to model with single-point closure. The database associated with the present paper is therefore expected to be a valuable contribution to the turbulence modelling community for both the benchmarking of existing turbulence models and the development of new models.

Conflict of interest

None.

Acknowledgement

The authors would like to acknowledge Rolls-Royce for the research funding and Imperial College HPC[1] for the computational resources made available for the simulations presented in the present paper.

Appendix A. Validation of the DNS code *incompact3d* for the simulation of buoyancy driven flows in differentially heated cavities

In order to demonstrate the ability of *incompact3d* to accurately predict the flow in differentially heated cavities, a comparison was carried out against the existing and acknowledged DNS simulation of Trias [19] in a 4:1 cavity with adiabatic boundary conditions on the horizontal walls. The simulation parameters used for the simulation with *incompact3d* are given in Table 4 below.

The dimensions of the domain as well as the time averaging window used are simply taken as it is from Trias et al. [19]. The excellent agreement with Trias et al. [19] of the present simulation is shown in Figs. 23 and 24.

Appendix B. Grid dependence study at $Ra = 1.58 \times 10^9$

As mentioned in Section 2.3, a grid dependence study specific to the simulation of the flow in a differentially heated cavity was carried out on three different meshes on a similar case presented in greater detail by Sebilleau [41]. The simulation parameters used are defined in Table 5 below. The comparison of the first and second order statistical moment obtained for the three different meshes is presented in Figs. 25 and 26 and shows an indisputable grid convergence of the results. The computed grid to Kolmogorov length scale ratio obtained in the present analysis is shown in Fig. 27. The values are of the same order as what is presented in Fig. 2 for the four simulations representing the core of the paper and therefore strengthen the confidence in the new data obtained at high Rayleigh number.

[1] http://www.imperial.ac.uk/admin-services/ict/self-service/research-support/hpc/.

References

[1] G.K. Batchelor, Heat transfer by free convection across a closed cavity between vertical boundaries at different temperatures, Quart. Appl. Math. 12 (1954) 209–233.
[2] J.W. Elder, Laminar free convection in a vertical slot, J. Fluid Mech. 23 (1965) 77–98.
[3] J.W. Elder, Turbulent free convection in a vertical slot, J. Fluid Mech. 23 (1965) 99–111.
[4] J.W. Elder, Numerical experiments with free convection in a vertical slot, J. Fluid Mech. 24 (1966) 823–843.
[5] J. Wilkes, S. Churchill, The finite difference computation of natural convection in a rectangular enclosure, Am. Inst. Chem. Eng. J. 12 (1966) 161–166.
[6] G. De Vahl Davis, Natural convection of air in a square cavity: a benchmark numerical solution, Int. J. Numer. Meth. Fluids 3 (1983) 249–264.
[7] D. Chenoweth, S. Paolucci, Natural convection in an enclosed vertical air layer with large horizontal temperature differences, J. Fluid Mech. 169 (1986) 173–210.
[8] S. Paolucci, D. Chenoweth, Transition to chaos in differentially heated vertical cavity, J. Fluid Mech. 201 (1989) 379–410.
[9] P. Le Quéré, M. Behnia, From onset of unsteadiness to chaos in a differentially heated square cavity, J. Fluid Mech. 359 (1998) 81–107.
[10] R.A.W.M. Henkes, P. Le Quéré, Three-dimensional transition of natural-convection flows, J. Fluid Mech. 319 (1996) 281–303.
[11] S. Xin, P. Le Quéré, Stability of two-dimensional (2d) natural convection flows in air-filled differentially heated cavities: 2d/3d disturbances, Fluid Dyn. Res. 44 (2012) 031419.
[12] S. Paolucci, Direct numerical simulation of two-dimensional turbulent natural convection in an enclosed cavity, J. Fluid Mech. 215 (1990) 229–262.
[13] S.H. Peng, L. Davidson, Numerical investigation of turbulent buoyant cavity using large eddy simulation, in: 3rd international Symposium on Heat and Mass Transfer, Aichi Shuppan, volume 3, 2000, pp. 737–744.
[14] S.-H. Peng, L. Davidson, Large eddy simulation for turbulent buoyant flow in a confined cavity, Int. J. Heat Fluid Flow 22 (2001) 323–331.
[15] Y.S. Tian, T.G. Karayiannis, Low turbulence natural convection in an air filled square cavity: Part I: The thermal and fluid flow fields, Int. J. Heat Mass Transf. 43 (2000) 849–866.
[16] Y.S. Tian, T.G. Karayiannis, Low turbulence natural convection in an air filled square cavity Part II: The turbulence quantities, Int. J. Heat Mass Transf. 43 (2000) 867–884.
[17] F. Ampofo, T.G. Karayiannis, Experimental benchmark data for turbulent natural convection in an air filled square cavity, Int. J. Heat Mass Transf. 46 (2003) 3551–3572.
[18] M. Soria, F.X. Trias, C.D. Pérez-Segarra, A. Oliva, Direct numerical simulation of a three-dimensional natural-convection flow in a differentially heated cavity of aspect ratio 4, Numer. Heat Transf. Part A: Appl. 45 (2004) 649–673.
[19] F.X. Trias, M. Soria, A. Oliva, C.D. Pérez-Segarra, Direct numerical simulations of two- and three-dimensional turbulent natural convection flows in a differentially heated cavity of aspect ratio 4, J. Fluid Mech. 586 (2007) 259.
[20] F.X. Trias, A. Gorobets, M. Soria, A. Oliva, Direct numerical simulation of a differentially heated cavity of aspect ratio 4 with Rayleigh numbers up to 10^{11} part I: numerical methods and time-averaged flow, Int. J. Heat Mass Transf. 53 (2010) 665–673.
[21] F.X. Trias, A. Gorobets, M. Soria, A. Oliva, Direct numerical simulation of a differentially heated cavity of aspect ratio 4 with Rayleigh numbers up to 10^{11} part II: heat transfer and flow dynamics, Int. J. Heat Mass Transf. 53 (2010) 674–683.
[22] D. Kizildag, F.X. Trias, I. Rodriguez, A. Oliva, Large eddy and direct numerical simulations of a turbulent water-filled differentially heated cavity of aspect ratio 5, Int. J. Heat Mass Transf. 77 (2014) 1084–1094.
[23] C. Bosshard, A. Dehbi, M. Deville, E. Leriche, R. Puragliesi, A. Soldati, Large eddy simulation of the differentially heated cubic cavity flow by the spectral element method, Comput. Fluids 86 (2013) 210–227.
[24] A. Dehbi, F. Han, J. Kalilainen, Large eddy simulations of flow inside a cubical differentially heated cavity under realistic boudary conditions, in: CFD for Nuclear Reactor Safety, Zurich, 2014.
[25] Z. Zhang, W. Chen, Z. Zhu, Y. Li, Numerical exploration of turbulent air natural-convection in a differentially heated square cavity at $Ra = 5.33 \times 10^9$, Heat Mass Transf. 50 (2014) 1737–1749.

[26] A. Sergent, S. Xin, P. Joubert, P. Le Quéré, J. Salat, F. Penot, Resolving the stratification discrepancy of turbulent natural convection in differentially heated air-filled cavities Part I: reference solutions using Chebyshev spectral methods, Int. J. Heat Fluid Flow 39 (2013) 1–14.
[27] R. Puragliesi, E. Leriche, Proper orthogonal decomposition of a fully confined cubical differentially heated cavity flow at rayleigh number $Ra = 10^9$, Comput. Fluids 61 (2012) 14–20.
[28] N.C. Markatos, K.A. Pericleous, Laminar and turbulent natural convection in an enclosed cavity, Int. J. Heat Mass Transf. 27 (1984) 755–772.
[29] K. Hanjalic, One-point closure models for buoyancy-driven turbulent flows, Annu. Rev. Fluid Mech. 34 (2002) 321–347.
[30] F. Dehoux, Y. Lecocq, S. Benhamadouche, R. Manceau, L.-E. Brizzi, Algebraic modeling of the turbulent heat fluxes using the elliptic blending approach −application to forced and mixed convection regimes, Turbul. Combust. 88 (2011) 77–100.
[31] F. Dehoux, Modélisation statistique des écoulements turbulents en convection forcée mixte et naturelle, Thesis, 2012.
[32] F. Dehoux, S. Benhamadouche, R. Manceau, Modelling turbulent heat fluxes using the elliptic blending approach for natural convection, in: Proc. 7th International Symposium on Turbulent Shear Flow Phenomena, Begel House Inc, 2011, p. 2014.
[33] T.A.M. Versteegh, F.T.M. Nieuwstadt, Turbulent budgets of natural convection in an infinite, differentially heated, vertical channel, Int. J. Heat Fluid Flow 19 (1998) 135–149.
[34] T.A.M. Versteegh, F.T.M. Nieuwstadt, A direct numerical simulation of natural convection between two infinite vertical differentially heated walls scaling laws and wall functions, Int. J. Heat Mass Transf. 42 (1999) 3673–3693.
[35] P. Kis, H. Herwig, Natural convection in a vertical plane channel: DNS results for high Grashof numbers, Heat Mass Transf. 50 (2014) 957–972.
[36] D.G. Barhaghi, L. Davidson, Natural convection boundary layer in a 5:1 cavity, Phys. Fluids 19 (2007) 125106.
[37] L. Soucasse, P. Rivière, A. Soufiani, Natural convection in a differentially heated cubical cavity under the effects of wall and molecular gas radiation at Rayleigh numbers up to 3×10^9, Int. J. Heat Mass Transf. 61 (2016) 510–530.
[38] D. Das, M. Roy, T. Basak, Studies on natural convection within enclosures of various (non-square) shapes: a review, Int. J. Heat Mass Transf. 106 (2017) 356–406.
[39] P. Wang, Y. Zhang, Z. Guo, Numerical study of three-dimensional natural convection in a cubical cavity at high Rayleigh numbers, Int. J. Heat Mass Transf. 113 (2017) 217–228.
[40] Y. Lecocq, Contribution à l'analyse et à la modélisation des écoulements turbulents en régime de convection mixte – Application à l'entreposage des déchets radioactifs, Ph.D. thesis, 2008.
[41] F. Sebilleau, Computational analysis of buoyancy driven flows across scales, Phd thesis, 2016.
[42] S. Laizet, E. Lamballais, High-order compact schemes for incompressible flows: a simple and efficient method with quasi-spectral accuracy, J. Comput. Phys. 228 (2009) 5989–6015.
[43] S. Laizet, N. Li, Incompact3d: a powerful tool to tackle turbulence problems with up to $\mathcal{O}(10^5)$ computational cores, Int. J. Numer. Meth. Fluids 67 (2011) 1735–1757.
[44] S.K. Lele, Compact finite difference schemes with spectral-like resolution, J. Comput. Phys. 103 (1992) 16–42.
[45] A.G. Kravchenko, P. Moin, On the effect of numerical errors in large eddy simulations of turbulent flows, J. Comput. Phys. 131 (1997) 310–322.
[46] C. Flageul, S. Benhamadouche, E. Lamballais, D. Laurence, DNS of turbulent channel flow with conjugate heat transfer: effect of thermal boundary conditions on the second moments and budgets, Int. J. Heat Fluid Flow 55 (2015) 34–44.
[47] L. Espath, L. Pinto, S. Laizet, J. Silvestrini, High-fidelity simulations of the lobe-and-cleft structures and the deposition map in particle-driven gravity currents, Phys. Fluids 27 (2015) 056604.
[48] H. Yu, N. Li, R.E. Ecke, Scaling in laminar natural convection in laterally heated cavities: is turbulence essential in the classical scaling of heat transfer?, Phys Rev. E Stat. Nonlin. Soft Matter Phys. 76 (2007) 026303.
[49] T. Tsuji, Y. Nagano, Characteristics of a turbulent natural convection boundary layer along a vertical flat plate, Int. J. Heat Mass Transf. 31 (1988) 1723–1734.
[50] T. Tsuji, Y. Nagano, Turbulence measurements in a natural convection boundary layer along a vertical flat plate, Int. J. Heat Mass Transf. 31 (1988) 2101–2111.
[51] W.K. George, S.P. Capp, A theory for natural convection turbulent boundary layers next to heated vertical surfaces, Int. J. Heat Mass Transf. 22 (1979) 813–826.
[52] M. Holling, H. Herwig, Asymptotic analysis of the near-wall region of turbulent natural convection flows, J. Fluid Mech. 541 (2005) 383–397.
[53] P.L. Betts, I.H. Bokhari, Experiments on turbulent natural convection in an enclosed tall cavity, Int. J. Heat Fluid Flow 21 (2000) 675–683.
[54] C.S. Ng, A. Ooi, D. Lohse, D. Chung, Vertical natural convection: application of the unifying theory of thermal convection, J. Fluid Mech. 764 (2015) 349–361.
[55] R. Boudjemadi, V. Maupu, D. Laurence, P. Le. Quéré, Budgets of turbulent stresses and fluxes in a vertical slot natural convection flow at Rayleigh $Ra = 10^5$ and 5.4×10^5, Int. J. Heat Fluid Flow 18 (1997) 70–79.